

EMFusion: Conditional Diffusion Framework for Trustworthy Frequency Selective EMF Forecasting in Wireless Networks

Zijiang Yan*¹, Yixiang Huang*², Jianhua Pei³, *Graduate Student Member, IEEE*,
Hina Tabassum⁴, *Senior Member, IEEE*, and Luca Chiaraviglio⁵, *Senior Member, IEEE*

Abstract—The rapid growth in wireless infrastructure has increased the need to accurately estimate and forecast electromagnetic field (EMF) levels to ensure ongoing compliance, assess potential health impacts, and support efficient network planning. While existing studies rely on univariate forecasting of wideband aggregate EMF data, frequency-selective multivariate forecasting is needed to capture the inter-operator and inter-frequency variations essential for proactive network planning. To this end, this paper introduces EMFusion, a conditional multivariate diffusion-based probabilistic forecasting framework that integrates diverse contextual factors (e.g., time of day, season, and holidays) while providing explicit uncertainty estimates. The proposed architecture features a residual U-Net backbone enhanced by a cross-attention mechanism that dynamically integrates external conditions to guide the generation process. Furthermore, EMFusion integrates an imputation-based sampling strategy that treats forecasting as a structural inpainting task, ensuring temporal coherence even with irregular measurements. Unlike standard point forecasters, EMFusion generates calibrated probabilistic prediction intervals directly from the learned conditional distribution, providing explicit uncertainty quantification essential for trustworthy decision-making. Numerical experiments conducted on frequency-selective EMF datasets demonstrate that EMFusion with the contextual information of working hours outperforms the baseline models with or without conditions. The EMFusion outperforms the best baseline by 23.85% in continuous ranked probability score (CRPS), 13.93% in normalized root mean square error, and reduces prediction CRPS error by 22.47%.

Index Terms—Electromagnetic field (EMF), EMF exposure forecasting, conditional diffusion model, probabilistic forecasting, uncertainty quantification, wireless communication network.

I. INTRODUCTION

The rapid proliferation of new wireless communication technologies, such as transmissions at higher frequencies, massive antennas, and reconfigurable intelligent surfaces (RISs), has led to an unprecedented increase in the radio-frequency (RF)-based electromagnetic field (EMF) sources [1], [2]. This technological surge has amplified public concerns regarding potential human health effects associated with EMF exposure [2]–[4]. Consequently, accurate EMF monitoring and forecast-

ing are becoming indispensable for regulatory compliance, network planning, and resource management [5], [6].

Existing studies primarily rely on stochastic modeling and optimization frameworks to manage exposure. Representative approaches include resource allocation and energy-efficiency maximization under EMF limits [7], [8], the integration of RIS to reduce exposure while maintaining service quality [9], and EMF-aware network planning through optimized base station (BS) placement and configuration [10], [11]. Operational strategies, such as exposure-conscious user association [12], beamforming optimization [13], and adaptive cross-layer protocols [14] further aim at exposure mitigation.

Beyond modeling-based strategies, some recent works have strengthened EMF measurement methodologies and long-term monitoring in the context of 5G deployment. For instance, [15] and [16] developed rigorous procedures for estimating the instantaneous maximum received power from 5G sources and refining exposure assessment at millimeter-wave frequencies. The IEC 62232:2025 standard [17] reports case studies evaluating EMF exposure across typical BS scenarios from 100 kHz to 300 GHz. Longitudinal monitoring data in [18] reveal a gradual increase in exposure at 3.6 GHz over two years in Greece, linked to expanding 5G infrastructure.

Despite these advances in EMF modeling and monitoring, EMF forecasting efforts remain limited. The handful of EMF forecasting studies remain primarily focused on univariate prediction of aggregate (wideband) exposure across large bandwidths [5], [19]–[22]. However, wideband exposure alone is often insufficient for regulatory oversight, active network planning, or proactive resource allocation. In practice, a frequency-selective breakdown is required to identify dominant exposure sources and quantify the contributions of specific technologies (e.g., 3G, 4G, and 5G deployments) and network operators. From a regulatory perspective, this granularity is essential. Environmental protection agencies must enforce maximum exposure limits at each frequency band across the territory to safeguard public health¹ Extending monitoring capabilities to frequency-selective forecasting would enable forward-looking compliance verification and transform periodic reporting from retrospective documentation into proactive decision support. Moreover, per-frequency forecasts could establish a feedback loop between regulatory oversight and network management, allowing operators to adjust spectrum allocation, transmission

Z. Yan and H. Tabassum are with the department of Electrical Engineering and Computer Science, York University, Toronto, Canada (e-mails: {zjiang, hinat}@yorku.ca). Y. Huang and J. Pei are with the School of Electrical and Electronic Engineering, Huazhong University of Science and Technology, Wuhan, China (e-mails: yxhuang@hust.edu.cn, jianhuapei98@gmail.com). J. Pei is also with the Central China Branch of State Grid Corporation of China, Wuhan, China. L. Chiaraviglio is with the Department of Electronic Engineering, University of Rome Tor Vergata, Rome, Italy (e-mail: luca.chiaraviglio@uniroma2.it). L. Chiaraviglio is also with the Consorzio Nazionale Interuniversitario per le Telecomunicazioni (CNIT), Parma, Italy. Z. Yan and Y. Huang contributed equally to this work and are co-first authors.

¹Simulation-based assessments submitted during site authorization are typically conservative and may differ from actual measured exposure levels, as operators often declare maximum radiated power, antenna tilting, or beamforming configurations that exceed those used in operation [4].

power, or deployment strategies, particularly in sensitive areas, before exposure limits are approached.

Although deep learning (DL) has achieved significant progress in time-series forecasting, conventional architectures such as recurrent neural networks (RNNs) and transformers are mainly designed for deterministic prediction. By producing single-point estimates, they often overlook intrinsic randomness, leading to overconfident forecasts and reduced robustness under noisy or dynamic conditions. Their autoregressive structure may also cause error accumulation over longer horizons. Recently, generative diffusion models (DMs) have emerged as a powerful probabilistic alternative, learning the full distribution of future trajectories through an iterative denoising process [23]–[25]. Beyond generating diverse and realistic forecasts, DMs support robust data imputation [26], [27] and flexible integration of contextual variables [28], making them well suited to capture the uncertainty and complexity of frequency-selective EMF dynamics.

Building on the need for *frequency-selective and probabilistic EMF forecasting under uncertainty*, this paper proposes *EMFusion*, a conditional diffusion model (CDM) for multivariate probabilistic forecasting of EMF exposure across multiple frequencies. The considered frequency-selective EMF datasets are inherently multivariate, as each timestamp comprises measurements across several frequency bands, wireless technologies, and network operators, forming a multidimensional observation vector. Modeling these jointly enables capturing shared temporal patterns, correlated behaviors, and coupled exposure dynamics. Accordingly, *EMFusion* models the joint distribution of multi-frequency EMF trajectories and provides built-in uncertainty quantification directly through its generative process, eliminating the need for post-hoc calibration.

To the best of our knowledge, conditional diffusion models have not been applied to time-series forecasting in wireless networks in general, nor to EMF forecasting in particular. The specific contributions of this paper can thus be summarized as:

- 1) The proposed *EMFusion* is based on a CDM for multivariate probabilistic forecasting of frequency-specific EMF exposure that allows the generation process to be guided by various contextual factors or conditions. *EMFusion* leverages contextual variables such as time of the day, day of the week, holiday/working days, working hours, and seasonal trends. This conditioning not only enhances the accuracy and relevance of the forecasts, but also allows for the generation of scenarios tailored to specific environmental states. The proposed architecture features a residual U-Net backbone enhanced by a cross-attention mechanism that dynamically integrates external conditions to guide the generation process. Furthermore, *EMFusion* integrates an imputation-based sampling strategy that treats forecasting as a structural inpainting task, ensuring temporal coherence even with irregular or missing EMF measurements.
- 2) Unlike conventional point forecasters that output a single trajectory, we propose a robust interval estimation framework based on the generative capabilities of *EMFusion*. By treating the ensemble of generated trajectories as samples from a conditional distribution, we employ Ker-

nel Density Estimation (KDE) to reconstruct continuous probability density functions at each time step. This approach enables the derivation of empirically calibrated prediction intervals without imposing parametric Gaussian assumptions, thereby achieving empirically validated coverage at prescribed confidence levels and providing trustworthy uncertainty quantification on EMF multivariate forecasting rather than simple point estimation.

- 3) *EMFusion* can be customized for both univariate and multivariate forecasting scenarios. Multivariate forecasting captures correlation across distinct network operators, transmission frequencies, and wireless technologies. Meanwhile, a univariate approach remains beneficial for scenarios where data or computational resources are limited, enabling fast, frequency-specific forecasts that are simpler to implement for localized optimization.
- 4) We conduct experiments on frequency-selective EMF exposure datasets spanning multiple narrowband channels in the frequency range of 9 kHz–6 GHz, thus covering major network operators in the Italy and cellular network technologies. Numerical results confirm the effectiveness of the conditional over unconditional *EMFusion*, and multivariate over univariate *EMFusion*. Among various exogenous conditions, we note that the working hour condition outperforms. Furthermore, the *EMFusion* outperforms the best baseline by around 23.85% continuous ranked probability score (CRPS), 13.93% normalized root mean square error (NRMSE) and reduces prediction CRPS error by 22.47%.

The remainder of this paper is organized as follows. Section II presents the existing state-of-the-art for TSF in wireless networks. Section III presents the architecture of the proposed multivariate *EMFusion* model. The experimental setup, data analysis, and visualizations are presented in Section IV followed by numerical results and discussions in Section V. Finally, Section VI concludes the paper.

II. RELATED WORK

TSF for wireless networks has evolved from classical statistical techniques to DL and, most recently, to generative AI. This subsection provides a review of existing state-of-the-art techniques for TSF and EMF forecasting in wireless networks.

1) *Statistical Methods for TSF*: Initial approaches to EMF exposure forecasting relied on classical time-series models. These included autoregressive models like ARIMA [43], as well as methods such as kernel ridge regression and support-vector regression. While computationally lightweight and interpretable, these techniques often assume stationarity and require significant manual feature engineering. Their linear parametrisation also limits their accuracy when the underlying drivers of EMF exposure interact non-linearly across multiple time scales. A representative approach is found in [44], who proposed a model that decomposes wide-band EMF radiation into three distinct components: the average exposure level, daily and half-daily periodic patterns (seasonal behavior), and the temporal correlation among residuals [44]. Their model effectively captured different behaviors between weekdays

TABLE I: Classification of deep learning models for wireless networks forecasting/prediction applications. **UV**: Univariate forecasting; **MV**: Multivariate forecasting; **Cond.**: External Conditions; **Imp.**: Imputation; **Trust.**: Trustworthiness.

| Domain | Ref. | Model | Target Dataset | UV/MV | Cond. | Imp. | Trust. |
|---------------------------|-----------------|------------------------------|-----------------------------------|--------------|---------------------------|------|--------|
| Network Traffic | [29] | MLP, MLPWD, SVM | Commercial LTE trial traffic | UV/MV | — | — | — |
| | [30] | VAR, RNN | LTE-A VoIP traffic | UV/MV | — | — | — |
| | [31] | LSTM RNN | Vodafone 4G throughput | UV | — | — | — |
| | [32] | Transformer | 5G/LTE O-RAN aggregate traffic | UV | — | — | — |
| | [33] | LSTM + XAI | 4G load and active-user datasets | UV | — | — | — |
| | [34] | VAR, LSTM | ubiquitous healthcare traffic | MV | — | — | — |
| Channel Prediction | [35] | Holt–Winters, LSTM | Real enterprise WLAN traffic | UV/MV | BS Traffic | — | — |
| | [36] | LSTM (SCP), RNN | Synthetic LEO mMIMO CSI | UV | — | — | — |
| QoS Prediction | [37] | Temporal Transformer | Real IoT smart-building datasets | UV/MV | — | ✓ | — |
| | [38] | BiLSTM–CNN | CDN video streaming QoE dataset | MV | — | — | — |
| | [39] | LSTM, Seq2Seq | Rural fixed-wireless LTE KPIs | MV | Weather | ✓ | — |
| | [40] | Diffusion + TCN | Real DTN-inspired sensor datasets | MV | Temperature | — | ✓ |
| EMF Exposure | [41] | LSTM, CNN | EMF measurements | UV | Population Density | — | — |
| | [19] | k-NN, XGBoost | EMF measurements | UV | Population Density | — | XAI |
| | [42] | CNN | Wideband RF-EMF | UV | — | — | — |
| | [20] | LSTM, RNN | Wideband RF-EMF | UV | — | — | — |
| | [21] | Transformer, CNN | Wideband RF-EMF | MV | — | — | — |
| | [5] | Patching, MLP | Wideband RF-EMF | UV | — | — | ✓ |
| | EMFusion | CDM + Cross attention | Frequency Selective RF-EMF | UV/MV | Time, Date, Season | ✓ | ✓ |

and weekends by applying separate autoregressive model for weekdays and Sunday, and the other autoregressive model for Saturday [44]. While effective, such methods are tailored to specific observed periodicities and struggle to generalize without manual recalibration.

2) *Deep Learning for TSF*: In this subsection, we classify DL approaches for TSF in wireless networks, including network traffic forecasting, QoS prediction, channel prediction, and EMF forecasting.

a) *Network Traffic Forecasting*: [29] compared Multi-Layer Perceptrons (MLP) as well as Support Vector Machines (SVM), to predict traffic in commercial Long-Term Evolution (LTE) networks. Similarly, [31] developed a univariate forecasting platform for 4G networks using LSTM and Recurrent Neural Networks (RNNs), demonstrating superiority over statistical baselines like ARIMA. More recent studies have shifted toward multivariate and interpretable models. [30] characterized LTE-Advanced Voice-over-IP metrics using Vector Autoregression (VAR) and supervised DL sliding-window frameworks. To enhance interpretability, [33] introduced AICHRONOLENS, an Explainable AI (XAI) framework that correlates temporal structures with LSTM error diagnoses. In the context of Software-Defined Networking, [34] utilized LSTM to model jointly evolving traffic flows for healthcare applications. Furthermore, for open radio access networks, [32] proposed a Transformer-based Autoformer architecture to predict aggregate cell traffic. While these methods achieve strong deterministic accuracy, they primarily focus on point forecasting. They generally lack explicit mechanisms for data imputation handling missing values and do not provide intrinsic uncertainty quantification essential for trustworthy

network planning.

b) *Channel Prediction*: Channel prediction is critical for mitigating aging in high-mobility scenarios. [35] benchmarked various models, including Holt-Winters and XGBoost, against LSTMs for enterprise Wireless Local Area Network traffic, analyzing spatio-temporal Access Point (AP) clustering. In satellite communications, [36] proposed a Satellite Channel Predictor based on LSTM units for Low Earth Orbit (LEO) massive Multiple-Input Multiple-Output (mMIMO) systems. Their approach outperformed Kalman filters and standard RNNs in multi-step Channel State Information (CSI) forecasting. Similar to traffic forecasting, these works rely on deterministic models and do not account for the confidence level of predictions, which is vital for robust resource allocation.

c) *Quality of Service (QoS) Prediction*: Forecasting QoS involves modeling complex dependencies. [38] introduced a hybrid bidirectional LSTM (BiLSTM) and Convolutional neural network (CNN) architecture for multivariate QoS forecasting in Content Delivery Networks (CDNs). [37] utilized a temporal Transformer encoder to predict QoS metrics in IoT networks, effectively capturing long-term dependencies that RNNs often miss. [39] investigated Sequence-to-Sequence (Seq2Seq) models for rural LTE Key Performance Indicators (KPIs), noting that exogenous features provided minimal gains due to short temporal dependencies.

d) *EMF Exposure Forecasting*: Research in EMF forecasting has progressed from spatial regression to time-series analysis. [19] focused on comparative regression using ensemble methods like Random Forest to rank urban factors affecting EMF levels. For temporal forecasting, [20] demonstrated that LSTMs outperform classical statistical models (e.g., ARIMA)

in long-term (over a 60-month period) for univariate EMF prediction. Recently, [21] demonstrated the effectiveness of 1-D CNNs in handling single-step and multi-step EMF forecasting tasks by leveraging translation invariance to identify periodicities in the data. Other research works also adapted CNN designs, utilizing architectures like Radial Basis Function Networks and Generalized Regression Neural Networks to model complex RF-EMF signals from emerging technologies like 5G [22]. Despite the aforementioned advancements, significant research gaps remain in the domain.

- 1) Existing EMF studies rely on univariate forecasting of aggregate EMF levels collected over a large bandwidth. Thus, they fail to capture the inter-operator and inter-frequency correlations essential for network planning.
- 2) Approaches like [5] rely on post-hoc calibration rather than learning the joint probability distribution directly. This decoupling can limit the expressiveness of the uncertainty representation. To address this, recent work has turned to distribution-free methods like conformal prediction. A notable example is EMFORECASTER [5], which integrates a powerful PatchTST backbone with a post-hoc conformal calibration layer. This two-stage pipeline delivers statistically valid prediction intervals for EMF levels. However, by decoupling uncertainty quantification from the primary sequence modeling, this approach is not directly applicable to multivariate frequency selective forecasting that adhere to the physical constraints and interdependencies across different frequency carriers, wireless technologies, and operators. Furthermore, EMFORECASTER [5] is designed for univariate forecasting, thus a large number of parallel models will be required to handle frequency selective forecasting.
- 3) Current works typically assume clean historical data, failing to address the frequent sensor outages and data gaps inherent in real-world EMF monitoring [21].

3) *Generative AI for TSF*: In recent years, generative models have emerged as a powerful paradigm within DL for TSF. Representative architectures include Variational Autoencoders (VAEs) [45], Generative Adversarial Networks (GANs) [46], [47], and, more recently, DMs [25], [48], which have gained remarkable attention for their ability to capture data uncertainty and generate high-fidelity forecasts. DMs, as latent-variable generative frameworks, learn complex data distributions via a dual process of progressive noise injection (the *forward diffusion*) and iterative denoising (the *reverse process*). More recently, DMs have been successfully adapted to time series data [49], [50], offering a flexible generative framework for learning intricate temporal dependencies and stochastic dynamics. While DiffTCN introduces probabilistic modeling, the majority of QoS research remains deterministic.

In the context of TSF, DMs are typically formulated as *conditional generative models*, where the goal is to produce future trajectories conditioned on past observations and optional contextual covariates [45], [49], [51]. During training, Gaussian noise is incrementally added to the ground-truth future sequence through the forward diffusion process, while a neural network, conditioned on historical context, is optimized

to learn the inverse mapping that progressively denoises the signal. At inference, forecasts are generated by iteratively sampling and denoising noise vectors, effectively drawing from the learned conditional distribution.

Compared to conventional deterministic or probabilistic models, DMs present several advantages:

- 1) DMs yield fully probabilistic forecasts, enabling uncertainty quantification through multiple stochastic samples and predicting extreme cases in terms of different EMF traffic flows, whereas deterministic models are disadvantaged in capturing uncertainty [52].
- 2) They maintain stable and well-behaved training dynamics, avoiding adversarial divergence;
- 3) They offer a highly modular design that allows flexible conditioning on exogenous factors such as seasonal indicators, control variables, or multimodal inputs [53]–[55].

Empirically, DMs demonstrate competitive or even state-of-the-art results across numerous TSF benchmarks [55]–[59], positioning them as a cornerstone of next-generation generative forecasting frameworks.

III. MULTIVARIATE EMFUSION: CONDITIONAL DM FOR FREQUENCY SELECTIVE EMF FORECASTING

This section details our methodology for multivariate EMF TSF leveraging a conditional DM. Given the sequence of historical EMF measurements and corresponding contextual factors, the goal is to model the conditional distribution of the future EMF values. The proposed model is then enhanced with imputation-based resampling to deal with real-world EMF logs where EMF measurements may be irregularly sampled or there are gaps or sensor outages. Before detailing the formal mathematical framework, we provide a conceptual overview of the three core pillars of the EMFusion architecture:

- **Diffusion Modeling as Iterative Refinement:** Unlike standard models that predict a single value, diffusion modeling treats forecasting as a process of systematic denoising. The model learns to reconstruct a structured, high-fidelity EMF signal from Gaussian noise through multiple refinement steps [23], [25].
- **Cross-Attention as Dynamic Weighting:** To ensure forecasts are context-aware, we utilize a cross-attention mechanism. This acts as a dynamic lens, allowing the model to selectively focus on specific historical patterns or external conditions (e.g., working hours or seasons) that are most relevant to the EMF time-series [23], [27].
- **Inpainting as Pattern Completion:** We frame the forecasting task as a structural inpainting problem. Much like filling in a missing piece of a photograph, the model treats future EMF values as the missing portion of a temporal image and utilizes the known "texture" of the past to complete the sequence realistically [26].

A. Multivariate Conditional Diffusion Model

We consider a multivariate time-series forecasting problem in which each observation $\mathbf{x}_k \in \mathbb{R}^N$ represents measurements from N variates or frequency channels at time k .

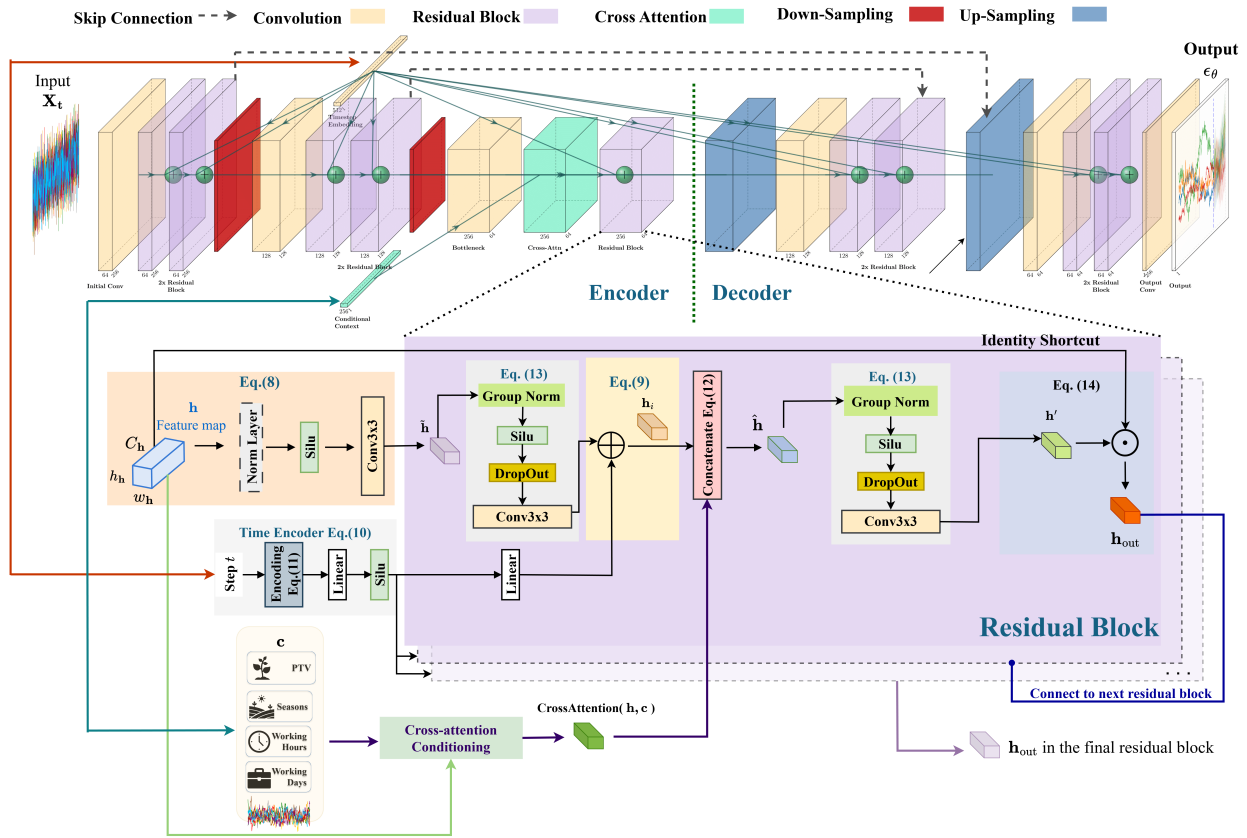


Fig. 1: The U-Net architecture used for EMFusion. The network processes a noisy input through a symmetric encoder-decoder path. Timestep embeddings are incorporated into the residual blocks, while external context is injected via a cross-attention block between the residual blocks of the encoder and decoder. The residual block architecture of EMFusion to estimate $\epsilon_{\theta}(\cdot)$.

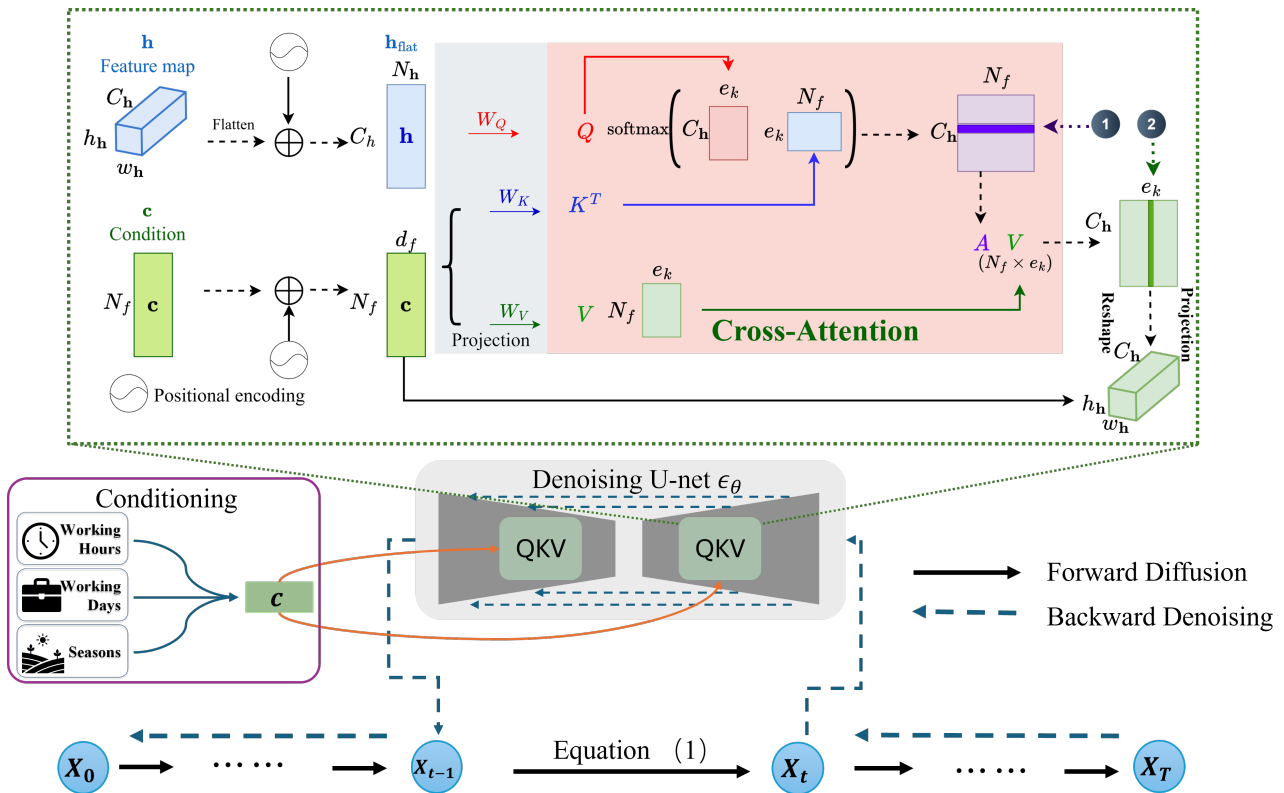


Fig. 2: EMFusion for multivariate frequency selective EMF forecasting with cross-attention.

Given a historical window of length H , denoted by $\mathbf{X}_{\text{past}} = (\mathbf{x}_{-(H+1)}, \dots, \mathbf{x}_0)$, the objective is to predict the future multichannel trajectory $\mathbf{X}_{\text{future}} = (\mathbf{x}_1, \dots, \mathbf{x}_F)$ over a forecast horizon F . To model the conditional distribution $p_\theta(\mathbf{X}_{\text{future}} | \mathbf{X}_{\text{past}}, \mathbf{c})$, we introduce an external condition vector \mathbf{c} , which may include calendar features, operational metadata, or other exogenous covariates. Unlike vectorized formulations, we treat the full future window as a matrix $\mathbf{X}_0 := [\mathbf{X}_{\text{past}}, \mathbf{X}_{\text{future}}] \in \mathbb{R}^{(H+F) \times N}$ and apply diffusion directly in this multivariate tensor space. This enables probabilistic forecasting while preserving the temporal-channel structure of the signal.

In the diffusion-based formulation, the forward noising process corrupts the clean \mathbf{X}_0 over T time steps according to the Markov transition process given by [23], [60]:

$$q(\mathbf{X}_t | \mathbf{X}_{t-1}) = \mathcal{N}(\sqrt{\alpha_t} \mathbf{X}_{t-1}, (1 - \alpha_t)\mathbf{I}), \quad (1)$$

which admits the closed-form marginal

$$q(\mathbf{X}_t | \mathbf{X}_0) = \mathcal{N}(\sqrt{\bar{\alpha}_t} \mathbf{X}_0, (1 - \bar{\alpha}_t)\mathbf{I}), \quad (2)$$

where $\alpha_t \in (0, 1]$ is a predefined noise schedule, \mathbf{I} denotes the identity matrix, and $\bar{\alpha}_t = \prod_{s=1}^t \alpha_s$, where α_s is the noise intensity of each step in the noise addition process. During training, noisy future samples can be directly sampled from \mathbf{X}_0 at any timestep t , i.e.,

$$\mathbf{X}_t = \sqrt{\bar{\alpha}_t} \mathbf{X}_0 + \sqrt{1 - \bar{\alpha}_t} \boldsymbol{\epsilon}, \quad \boldsymbol{\epsilon} \sim \mathcal{N}(0, \mathbf{I}), \quad (3)$$

with $\boldsymbol{\epsilon} \in \mathbb{R}^{(H+F) \times N}$ containing i.i.d. Gaussian noise.

The training objective minimizes the discrepancy between the true noise $\boldsymbol{\epsilon}$ and the network-predicted noise $\boldsymbol{\epsilon}_\theta(\mathbf{X}_t, t, \mathbf{c})$ using a mean-squared error loss:

$$L(\theta) = \mathbb{E}_{t, \mathbf{X}_0, \boldsymbol{\epsilon}} \left[\left\| \boldsymbol{\epsilon} - \boldsymbol{\epsilon}_\theta(\sqrt{\bar{\alpha}_t} \mathbf{X}_0 + \sqrt{1 - \bar{\alpha}_t} \boldsymbol{\epsilon}, t, \mathbf{c}) \right\|^2 \right]. \quad (4)$$

The reverse diffusion process serves as the generative mechanism for forecasting. The conditional reverse diffusion process predicts the distribution $p_\theta(\mathbf{X}_{t-1} | \mathbf{X}_t, \mathbf{c})$, of the less noisy state \mathbf{X}_{t-1} given the current noisy state \mathbf{X}_t and the conditioning information \mathbf{c} . It learns to reconstruct the original signal \mathbf{X}_0 by iteratively denoising the noisy samples, starting from pure noise $\mathbf{X}_T \sim \mathcal{N}(0, \mathbf{I})$. A neural network $\boldsymbol{\epsilon}_\theta(\mathbf{X}_t, t, \mathbf{c})$ is employed to approximate the reverse transition distribution $p_\theta(\mathbf{X}_{t-1} | \mathbf{X}_t, \mathbf{c})$ by predicting the noise component $\boldsymbol{\epsilon}$ that was added at step t . This noise prediction network takes the noisy data \mathbf{X}_t , the current timestep t , and the conditioning vector \mathbf{c} to predict the following conditional distribution:

$$p_\theta(\mathbf{X}_{t-1} | \mathbf{X}_t, \mathbf{c}) = \mathcal{N}(\boldsymbol{\mu}_\theta(\mathbf{X}_t, t, \mathbf{c}), \boldsymbol{\Sigma}_t(\mathbf{X}_t, t, \mathbf{c})), \quad (5)$$

where the mean computed from $\boldsymbol{\epsilon}_\theta$ is given by:

$$\boldsymbol{\mu}_\theta(\mathbf{X}_t, t, \mathbf{c}) = \frac{1}{\sqrt{\alpha_t}} \left(\mathbf{X}_t - \frac{1 - \alpha_t}{\sqrt{1 - \bar{\alpha}_t}} \boldsymbol{\epsilon}_\theta(\mathbf{X}_t, t, \mathbf{c}) \right). \quad (6)$$

and \mathbf{c} encapsulates features from the dataset, such as `Italy_WorkingDay`, `Italy_WorkingHour`, and `Italy_Season`, which depict factors influencing EMF variations [58], [59]. By conditioning the noise prediction on \mathbf{c} , the model learns to generate EMF trajectories consistent with temporal continuity and relevant external dependencies.

Algorithm 1: DDPM Training for Multivariate Forecasting with Cross-Attention

Input: $\mathbf{X}_0 = [\mathbf{X}_{\text{past}}, \mathbf{X}_{\text{future}}]$, conditions \mathbf{c}
Output: Learned parameters θ
 Sample $t \sim \mathcal{U}\{1, \dots, T\}$ and noise $\boldsymbol{\epsilon} \sim \mathcal{N}(0, \mathbf{I})$;
 Generate noisy sequence: $\mathbf{X}_t = \sqrt{\bar{\alpha}_t} \mathbf{X}_0 + \sqrt{1 - \bar{\alpha}_t} \boldsymbol{\epsilon}$;
 Pass \mathbf{X}_t and t through U-Net;
 Time series t embedding
for each cross-attention block **do**
 Positional encoding computed by Eq (15);
 Compute $Q = \mathbf{h}_{\text{nat}} W_Q$, $K = \mathbf{c} W_K$, $V = \mathbf{c} W_V$;
 Compute Attention = $\text{Softmax}(QK^\top / \sqrt{e_k})V$;
 Update feature map: $\mathbf{h} \leftarrow \mathbf{h} + \text{Attn}$;
end
 Predict noise with Cross Attention by Eq (12):
 $\hat{\boldsymbol{\epsilon}}_\theta = \boldsymbol{\epsilon}_\theta(\mathbf{X}_t, t, \mathbf{c})$;
 Update parameters by minimizing $\mathcal{L}(\theta) = \|\boldsymbol{\epsilon} - \hat{\boldsymbol{\epsilon}}_\theta\|_2^2$;

This formulation enables a fully multivariate, conditionally guided reverse diffusion process in which \mathbf{X}_t is iteratively denoised using both the historical multichannel window \mathbf{X}_{past} and the external condition vector \mathbf{c} .

During inference, a classifier-free guidance (CFG) mechanism [23], [61] steers the generation process. The final noise prediction is obtained by combining the conditional and unconditional outputs of the denoising network:

$$\hat{\boldsymbol{\epsilon}}_\theta(\mathbf{X}_t, t, \mathbf{c}) = (1 + s_c) \boldsymbol{\epsilon}_\theta(\mathbf{X}_t, t, \mathbf{c}) - s_c \boldsymbol{\epsilon}_\theta(\mathbf{X}_t, t, \emptyset), \quad (7)$$

where s_c is the guidance scale controlling the adherence to the conditioning input \mathbf{c} , and \emptyset represents an unconditional prediction. In conditional TSF, positive CFG scales often over-concentrate the posterior, which narrows prediction intervals. Since our model already injects conditioning via cross-attention, we found $s_c = 0$ is the best via hyperparameter tuning. This conditional diffusion formulation provides the theoretical basis for our model.

B. Model Architecture and Cross-Attention Integration

We employ a U-Net backbone for the noise-prediction network $\boldsymbol{\epsilon}_\theta$. As shown in Fig. 1, the U-Net is a deep neural network with multiple residual blocks. The encoder and decoder are symmetric structure, consisting of the same number of residual blocks and additional downsampling or upsampling block. Each residual block contains convolution to capture local details of the long series, with the input \mathbf{X}_t , condition \mathbf{c} , and time step t . The input multivariate \mathbf{X}_0 passes through the U-Net and is processed by residual block to an intermediate feature map \mathbf{h} (with dimensions $C_h \times h_h \times w_h$), while $\mathbf{h} = \mathbf{X}_t$ in the first layer. Here, C_h is the number of channels in the convolutional layer, h_h and w_h are the spatial height and width of the feature map, respectively.

1) *Residual Block with Time-Step Embedding:* The core of the $\boldsymbol{\epsilon}_\theta$ network is a stack of residual blocks that progressively refine the feature maps. As shown in Fig. 1, each residual block applies normalization, nonlinearity, convolution, and time step conditioning, followed by a residual shortcut. Given an input feature map \mathbf{h} from the previous layer, the block

Algorithm 2: DDPM Inference for Multivariate Forecasting with Cross-Attention and Masked Imputation

Input: \mathbf{X}_{past} , mask Ω , conditions \mathbf{c} , unknown future window $\mathbf{X}_{\text{future}}$

Output: Sampled future trajectory $\hat{\mathbf{X}}_{\text{future}}$

Initialize $\mathbf{X}_T \in \mathbb{R}^{(H+F) \times N} \sim \mathcal{N}(0, I)$,

$\mathbf{X}_0 = [\mathbf{X}_{\text{past}}, \mathbf{X}_{\text{future}}]$;

for $t = T$ to 1 **do**

Time series t embedding

Positional encoding computed by Eq (15);

Predict noise with Cross Attention by Eq (12);

$\hat{\epsilon}_\theta = \epsilon_\theta(\mathbf{X}_t, t, \mathbf{c})$;

Sample $\mathbf{z} \sim \mathcal{N}(0, I)$ if $t > 1$, else $\mathbf{z} = 0$;

Compute one step denoised estimate:

$\mathbf{X}'_{t-1} = \frac{1}{\sqrt{\alpha_t}} \left(\mathbf{X}_t - \frac{1-\alpha_t}{\sqrt{1-\alpha_t}} \hat{\epsilon}_\theta \right) + \sigma_t \mathbf{z}$;

Sample $\epsilon \sim \mathcal{N}(0, I)$ for \mathbf{X}_{past} if $t > 1$, else $\epsilon = 0$;

Add noise to \mathbf{X}_0 : $\mathbf{X}_{\text{obs}} = \sqrt{\alpha_t} \mathbf{X}_0 + \sqrt{1-\alpha_t} \epsilon$;

Clamp observed values (imputation step):

$\hat{\mathbf{X}}_{t-1} = \Omega \odot \mathbf{X}_{\text{obs}} + (1 - \Omega) \odot \mathbf{X}'_{t-1}$;

end

Extract $\hat{\mathbf{X}}_{\text{future}}$ from \mathbf{X}_0 ;

first applies Group Normalization and a Sigmoid Linear Unit (SiLU) activation, followed by a 3×3 convolution, i.e., [63]:

$$\tilde{\mathbf{h}} = \text{Conv}_1(\sigma(\text{GN}(\mathbf{h}))), \quad (8)$$

where $\text{GN}(\cdot)$ denotes GroupNorm, $\sigma(\cdot)$ is the SiLU activation, and Conv_1 is a 3×3 convolution.

A critical component of the block is the injection of the diffusion step embedding. The global timestep embedding \mathbf{t}^e is passed through a block-specific linear layer and then added to the intermediate feature map:

$$\mathbf{h}_i = \tilde{\mathbf{h}} + \text{Linear}_t(\sigma(\mathbf{t}^e)), \quad (9)$$

where Linear_t maps $\mathbf{t}^e \in \mathbb{R}^{d_{\text{embed}}}$ to the channel dimension of the block, and the result is broadcast across spatial dimensions. This makes the block's behavior explicitly adaptive to the current diffusion step t .

To incorporate the diffusion timestep to the residual block and enrich its effective information, a sinusoidal time embedding is employed to expand its dimension. The timestep t is first mapped into a positional embedding vector \mathbf{t}^e as

$$\mathbf{t}^e = \text{Concat} \left(\begin{bmatrix} \cos(t \cdot \omega_0), \dots, \cos\left(t \cdot \omega_{\frac{d}{2}-1}\right) \\ \sin(t \cdot \omega_0), \dots, \sin\left(t \cdot \omega_{\frac{d}{2}-1}\right) \end{bmatrix} \right), \quad (10)$$

For a given dimension index m where $0 \leq m < C_h/2$, the frequencies are defined as follows:

$$\omega_m = \exp(-\ln(10000) \cdot \frac{2m}{C_h}) \quad (11)$$

We integrate condition \mathbf{c} into the feature map using cross-attention operation as shown below (more details of the cross-attention are given in the following subsection and Fig. 2):

$$\hat{\mathbf{h}} = \mathbf{h}_i + \text{CrossAttention}(\mathbf{h}, \mathbf{c}). \quad (12)$$

The updated feature map $\hat{\mathbf{h}}$ is then processed by a second sequence of operations, GroupNorm, SiLU, dropout, and another 3×3 convolution [63]:

$$\mathbf{h}' = \text{Conv}_2(\text{Dropout}(\sigma(\text{GN}(\hat{\mathbf{h}})))). \quad (13)$$

Finally, a residual shortcut is applied as [64]:

$$\mathbf{h}_{\text{out}} = \mathbf{h}' + \text{Shortcut}(\mathbf{h}), \quad (14)$$

where Shortcut is the identity mapping for feature mining and convolution operation for up sampling and down sampling. By stacking these modules in the encoder, the series is processed shorter and the convolution channels increase, so that abstract temporal and spatial information are extracted.

2) *Cross-Attention Module*: To integrate conditioning information, instead of simple concatenation, we use cross-attention modules at multiple layers in both the encoder and decoder, as depicted in Fig. 2. This allows the model to dynamically attend to the most relevant parts of the conditioning information at different stages of processing and across different temporal scales. The condition tensor \mathbf{c} (with dimensions $N_f \times d_f$) and the intermediate feature map \mathbf{h} are two inputs of the cross-attention module. Note that N_f is the sequence length of the condition and d_f is its feature dimension.

To compute the attention, the 3D feature map \mathbf{h} is first flattened into a 2D tensor, \mathbf{h}_{flat} , with shape (C_h, N_h) , where $N_h = h_h \cdot w_h$. Since cross-attention calculation basically contains linear connection without recurrence, it's important to fully make use of the order of the sequence. Positional encoding adds positional information to \mathbf{c} and \mathbf{h}_{flat} , which helps the module extract temporal and spatial correlations. Consequently, we add positional encoding to \mathbf{c} and \mathbf{h}_{flat} according to [65]:

$$\mathbf{c} \leftarrow \mathbf{c} + PE(\mathbf{c}) \in \mathbb{R}^{N_f \times d_f} \quad (15)$$

$$\mathbf{h}_{\text{flat}} \leftarrow \mathbf{h}_{\text{flat}} + PE(\mathbf{h}_{\text{flat}}) \in \mathbb{R}^{C_h \times N_h} \quad (16)$$

$$PE(\cdot) = \begin{cases} PE_{(p, 2i)} = \sin(p/10000^{2i/d_{\text{series}}}), \\ PE_{(p, 2i+1)} = \cos(p/10000^{2i/d_{\text{series}}}), \end{cases} \quad (17)$$

where p and i denote the position and the dimension index of the input series, respectively, and d_{series} is the embedding dimension of the sequence.

The cross-attention module operates between the feature map and the conditional embeddings, allowing the model to explicitly learn their correlations and dynamically modulate its representations based on the provided conditions. Its calculation is based on QKV where the Queries (Q) are projected from this flattened feature map, while the Keys (K) and Values (V) are projected from the conditioning tensor \mathbf{c} , i.e.,

$$Q = \mathbf{h}_{\text{flat}} W_Q, \quad K = \mathbf{c} W_K, \quad V = \mathbf{c} W_V \quad (18)$$

where W_Q , W_K , and W_V are learnable weight matrices [23], [66]. The attention matrix A and the final output are calculated using the standard scaled dot-product attention mechanism:

$$\text{CrossAttention}(\mathbf{h}, \mathbf{c}) = \text{Softmax} \left(\frac{QK^T}{\sqrt{e_k}} \right) V = AV, \quad (19)$$

TABLE II: Frequency f (MHz) allocation for mobile operators and technology band used in the Italian dataset. Each entry shows the antenna factor (α_f) in dB m⁻¹ from Keysight N6850A calibration [62].

| | | |
|--------------|------------------------------|--|
| Operators | $\mathcal{F}_{\text{Iliad}}$ | 763.0 (32.8), 1835.0 (31.2), 2150.0 (31.9), 2635.0 (33.2), 3630.0 (36.6) |
| | \mathcal{F}_{TIM} | 773.0 (32.9), 806.0 (33.3), 935.0 (34.7), 2137.0 (31.8), 2137.5 (31.8), 2662.0 (33.3), 2662.5 (33.3), 3760.0 (36.9), 3468.0 (36.0), 3468.5 (36.0), 3469.0 (36.0), 3568.0 (36.3), 3568.5 (36.3) |
| | \mathcal{F}_{VF} | 783.0 (33.0), 816.0 (33.4), 945.0 (34.8), 1870.0 (31.0), 2162.0 (31.9), 2162.5 (31.9), 2647.0 (33.2), 2647.5 (33.2), 3680.0 (36.7) |
| | \mathcal{F}_{W3} | 796.0 (33.2), 955.0 (34.9), 1850.0 (30.9), 2120.0 (31.7), 2585.0 (33.0), 2680.0 (33.4), 3610.0 (36.5) |
| Technologies | $\mathcal{F}_{2\text{G}}$ | 935.0 (34.7), 945.0 (34.8), 955.0 (34.9) |
| | $\mathcal{F}_{3\text{G}}$ | 2120.0 (31.7), 2137.0 (31.8), 2137.5 (31.8), 2150.0 (31.9), 2162.0 (31.9), 2162.5 (31.9) |
| | $\mathcal{F}_{4\text{G}}$ | 763.0 (32.8), 773.0 (32.9), 783.0 (33.0), 796.0 (33.2), 806.0 (33.3), 816.0 (33.4), 1835.0 (31.2), 1850.0 (30.9), 1870.0 (31.0), 2585.0 (33.0), 2635.0 (33.2), 2647.0 (33.2), 2647.5 (33.2), 2662.0 (33.3), 2662.5 (33.3), 2680.0 (33.4) |
| | $\mathcal{F}_{5\text{G}}$ | 3468.0 (36.0), 3468.5 (36.0), 3469.0 (36.0), 3568.0 (36.3), 3568.5 (36.3), 3610.0 (36.5), 3630.0 (36.6), 3680.0 (36.7), 3760.0 (36.9) |

where e_k is the dimension of the keys (and queries), used for scaling. According to ① in Fig. 2, a single row of the attention matrix A represents the set of attention weights that one specific element from the flattened feature map \mathbf{h}_{flat} (represented by a row of Q) pays to all N_f elements of the condition vector \mathbf{c} (represented by the rows of K). ② in Fig. 2 shows a column of the value V that corresponds to a feature map weighted by the attention in A [67]. The output of this operation, AV , represents the contextually relevant information from \mathbf{c} , weighted according to its relevance to \mathbf{h} . This output is then reshaped and projected to match the original feature map’s dimensions ($C_h \times h_h \times w_h$). This result is finally added back to the original feature map \mathbf{h} via a residual connection, which is shown in the previous section:

$$\mathbf{h}' = \mathbf{h} + \text{CrossAttention}(\mathbf{h}, \mathbf{c}).$$

In this context, $\text{CrossAttention}(\cdot)$ in Eq. (12) represents the full module’s operation, including the final reshape and projection steps shown in the diagram. According to ② in Fig. 2, a single column of the final output (AV) is the new vector representation for that specific feature map element. It is calculated as the weighted sum of all N_f rows of the Value matrix V . The weights used for this sum are the attention scores from the corresponding row of A .

C. EMFusion Training and Inference

The cross-attention integrated U-Net learns to predict noise in the training phase as Algorithm 1. Given the full window $\mathbf{X}_0 = [\mathbf{X}_{\text{past}}, \mathbf{X}_{\text{future}}]$ and the conditions \mathbf{c} , the first step is to randomly choose a $t \sim \mathcal{U}\{1, \dots, T\}$ and noise $\epsilon \sim \mathcal{N}(0, I)$ to add noise to the original sequence \mathbf{X}_0 by using Eq. (3): $\mathbf{X}_t = \sqrt{\alpha_t} \mathbf{X}_0 + \sqrt{1 - \alpha_t} \epsilon$. The task of the U-Net is to learn the ability to predict ϵ given $\mathbf{X}_t, t, \mathbf{c}$. Pass \mathbf{X}_t through U-Net and generate intermediate feature map \mathbf{h} . Then embed positional information to \mathbf{c} and \mathbf{X}_0 and calculate cross-attention between \mathbf{h} and \mathbf{c} when going through cross-attention blocks.

Subsequently the output noise $\hat{\epsilon}_\theta$ is the same dimension as ϵ . By minimizing MSE loss $\mathcal{L}(\theta) = \|\epsilon - \hat{\epsilon}_\theta\|_2^2$, the model updates itself and learn to predict noise based on any t . Then the well-trained model participates in the denoising process in the inference phase by predicting noise $\hat{\epsilon}_\theta = \epsilon_\theta(\mathbf{X}_t, t, \mathbf{c})$ at each step t and the conditions are input through cross-attention module, as shown in Algorithm 2.

D. Imputation-Based Sampling at the Inference

In practical EMF monitoring, historical measurements are often uneven, partially observed, or corrupted due to sensor outages, data-handling issues, and privacy-related filtering, resulting in time series with substantial gaps and irregular sampling. Such incomplete inputs limit the effectiveness of pure conditional forecasting, which assumes fully reliable past observations. An imputation-based diffusion formulation addresses this limitation by treating both missing past values and all future values as unobserved entries of a single masked sequence. During the DDPM reverse process, the model performs principled generative inpainting—reconstructing irregular or missing segments of the past while simultaneously generating future values under the same probabilistic dynamics. Since past and future EMF measurements lie on the same underlying temporal manifold, casting forecasting as structured inpainting enables the model to learn cross-temporal dependencies across the entire sequence.

To handle both forecasting and imputation within a unified framework, we adopt a masked conditional DDPM that models the full sequence $\mathbf{X}_0 = [\mathbf{X}_{\text{past}}, \mathbf{X}_{\text{future}}]$ under partial observations. That is, the model receives a concatenated input sequence \mathbf{X}_0 consisting of a known historical window \mathbf{X}_{past} and an unknown future window $\mathbf{X}_{\text{future}}$ that is initially masked. The objective is to infer the missing future segment in a manner that is probabilistically consistent with \mathbf{X}_{past} . The algorithmic realization is summarized in Algorithm 2.

Let Ω denotes a binary observation mask (for the i -th element, $\Omega_i = 1$ for observed entries and $\Omega_i = 0$ for missing

ones), and let $\mathbf{X}_{\text{obs}} = \sqrt{\alpha_t} \mathbf{X}_0 + \sqrt{1 - \alpha_t} \boldsymbol{\epsilon}$, $\boldsymbol{\epsilon} \sim \mathcal{N}(0, \mathbf{I})$, denotes the available measurements. As in standard diffusion models, the forward process gradually perturbs the clean sequence \mathbf{X}_0 with Gaussian noise as in (3), while the model learns a masked conditional reverse process, i.e., (5) still applies by adding conditions on \mathbf{c} . The noisy sequence is processed through the conditional U-Net $\epsilon_\theta(\mathbf{X}_t, t, \mathbf{c})$ to obtain a one-step denoised estimate of the entire trajectory, denoted as $\hat{\mathbf{X}}_{t-1}$. After each denoising step, the observed entries are clamped to their known values to ensure consistency:

$$\hat{\mathbf{X}}_{t-1} = \Omega \odot \mathbf{X}_{\text{obs}} + (1 - \Omega) \odot \mathbf{X}'_{t-1}, \quad (20)$$

where $\hat{\mathbf{X}}_{t-1}$ denotes the model's predicted denoised sample at timestep $t - 1$.

$$\hat{\mathbf{X}}_{t-1} = \frac{1}{\sqrt{\alpha_t}} \left(\mathbf{X}_t - \frac{1 - \alpha_t}{\sqrt{1 - \alpha_t}} \hat{\boldsymbol{\epsilon}}_\theta \right) + \sigma_t \mathbf{z} \quad (21)$$

After T iterations of the denoising process, a predicted sequence $\hat{\mathbf{X}}_{\text{future}}$ can be obtained from $\hat{\mathbf{X}}_0$. This mechanism enables the DM to impute with past values and generate future trajectories within the same sampling procedure. The training objective follows the standard noise-prediction loss as in (4) with masked conditioning. If we sample \hat{N} times, a set of \hat{N} predicted sequences $\mathbf{S} = \{\hat{\mathbf{X}}_{\text{future}}^i\}_{i=1, \dots, \hat{N}}$ is ready for probabilistic interval construction which is explained next.

E. Probabilistic Interval Construction

Once EMFusion generates an ensemble of \hat{N} future EMF trajectories $\mathbf{S} = \{\hat{\mathbf{X}}_{\text{future}}^i\}_{i=1}^{\hat{N}} \in \mathbb{R}^{\hat{N} \times F}$ for each monitored carrier (e.g., individual 2G, 3G, 4G, and 5G carriers across multiple operators), the samples at forecast horizon $k \in \{1, \dots, F\}$ are given by $\mathbf{Z}_k = \{z_k^1, \dots, z_k^{\hat{N}}\}$. These samples are interpreted as Monte-Carlo draws from the learned conditional predictive distribution. A smooth estimate of the predictive density at horizon k is obtained via Kernel Density Estimation (KDE) as shown below:

$$\hat{f}_k(z) = \frac{1}{\hat{N} s_p} \sum_{i=1}^{\hat{N}} K\left(\frac{z - z_k^i}{s_p}\right), \quad (22)$$

where $K(\cdot)$ denotes the Gaussian kernel function and s_p is the bandwidth parameter controlling the bias-variance trade-off. The corresponding cumulative distribution function is $\hat{F}_k(z) = \int_{-\infty}^z \hat{f}_k(t) dt$. For a target confidence level γ , define $\underline{\alpha} = \frac{1-\gamma}{2}$, $\bar{\alpha} = 1 - \underline{\alpha}$. The prediction interval based on the estimated density is given by:

$$PI_\gamma = \left[\hat{F}_k^{-1}(\underline{\alpha}), \hat{F}_k^{-1}(\bar{\alpha}) \right]. \quad (23)$$

In practical implementation, instead of explicitly evaluating the KDE and numerically inverting the CDF, the required quantiles are computed directly from the ordered ensemble samples. Let $z_k^{(1)} \leq \dots \leq z_k^{(\hat{N})}$ denotes the order statistics of \mathbf{Z}_k . Let us define $\ell = \lceil \underline{\alpha} \hat{N} \rceil$, $u = \lceil \bar{\alpha} \hat{N} \rceil$. The empirical prediction interval is then given by $PI_\gamma = [L_k, U_k] = [z_k^{(\ell)}, z_k^{(u)}]$. As the ensemble size \hat{N} increases, the empirical quantiles

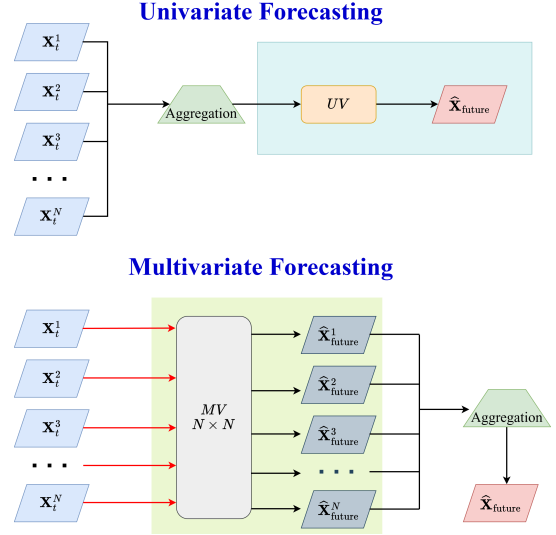


Fig. 3: Comparison of univariate (UV) and multivariate (MV) forecasting strategies for EMF time-series across N features.

converge to those of the underlying distribution, ensuring statistically consistent and efficient uncertainty estimation.

F. Univariate Forecasting: A Special Case

As illustrated in Fig. 3, Univariate forecasting illustrates the aggregate-then-learn paradigm, where multiple time series are first aggregated before applying the forecasting model. Multivariate forecasting the learn-then-aggregate paradigm, where forecasts are generated for each frequency series individually and then aggregated. In the EMFusion framework, the main differences between the univariate and multivariate instantiations of EMFusion are confined to the input dimensionality and the associated architectural hyperparameters. In the multivariate setting ($N > 1$), the input \mathbf{X}_0 is treated as a 2-D tensor, processed via 2-D convolutional layers to simultaneously capture temporal evolution and inter-frequency correlations. Conversely, the univariate configuration ($N = 1$) utilizes 1-D convolutions, focusing exclusively on temporal dynamics. In the univariate setting, the model receives a single narrow-band EMF time series and the input tensor is of shape $(B, H, 1)$, where B is the batch size and H is the look-back length, thus we employ 1-D convolutions. In the multivariate setting, the input at each time step lead to an input tensor of shape (B, H, N) and 2-D convolutions acting jointly on time and frequency. When computing cross-attention, the univariate uses a single hidden channel $h_h = 1$ in the value projection (effectively attending only along time), whereas the multivariate sets $h_h > 1$ so that attention can propagate information both temporally and across bands.

IV. DATA SPECIFICATIONS AND ANALYSIS

This section details dataset specifications including the measurement set-up, received power (dBm) to electric-field (Volts per meter) conversion, and the external conditioning factors. The top two plots in Fig. 4 show the time evolution²

²The data were collected at the University Hospital Tor Vergata in Rome, Italy, from 2023-07-26 16:49:02 to 2024-03-11 05:08:28.

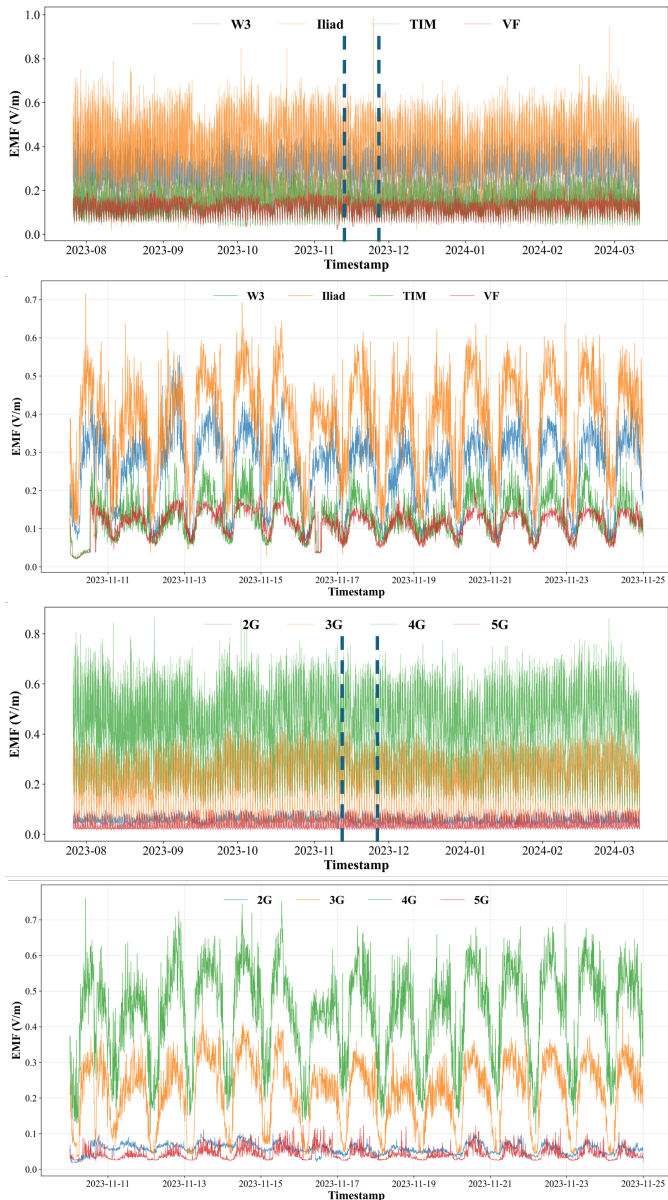


Fig. 4: EMF levels in Italian dataset, as a function of network operators (1,2) and cellular technologies (3,4). The plots (1,3) display the 8-month trend (Aug 2023 – Mar 2024), while the plots (2,4) show enlarged 14-day daily trend.

of operator-specific EMF levels in the Italian dataset. The operator-wise difference in EMF levels is notable. Iliad systematically dominates the total exposure, with a typical peak at 0.8 v/m. W3 provides the second-largest contribution on EMF, while TIM and VF remain consistently lower, with most values below 0.3 V/m. This suggests antenna being placed in the University hospital or a configuration that produced a stronger signal at the specific point of measurement in favour of Iliad. Moreover, while the other operators display broadly similar deployment and load patterns, Iliad follows a more independent deployment and load profile, with a narrower spectrum allocation in the mid-band 5G frequencies compared to the other operators.

On the other hand, the bottom two plots in Fig. 4 depict that

the EMF level from 4G clearly dominates the total EMF levels from 2G, 3G, or 5G technologies, both in terms of average level and short-term variability, with typical peaks reaching 0.8 V/m. The 3G contribution is noticeably smaller but still non-negligible, while 2G and 5G produce the lowest fields, generally below 0.1 V/m except for a few isolated peaks. This trend is likely due to the sparse deployment of both 2G and 5G technologies and widespread deployment of 4G at the time of measurements. Both operator-wise and technology-wise display the recurrent daily cycle and stable behaviour over the months. According to Fig. 5, 4G is only weakly correlated with the other technologies ($\rho \leq 0.19$), whereas 5G exhibits a moderate correlation with 2G and 3G. This behavior is consistent with the technological innovations introduced in 4G and 5G with respect to legacy generations, such as active antennas, beamforming, MIMO, and time-division duplexing.

A. Dataset Specifications

The received power measurements were collected continuously from July 26, 2023 to March 10, 2024 across 29 frequency channels spanning from 9 kHz - 6GHz. The dataset is then organized according to the predefined frequency bands of major Italian network operators and the corresponding cellular technologies. Table II summarizes the frequency allocations used by each operator and technology.

1) *EMF Monitoring Set-up*: The EMF monitoring chain couples an omnidirectional antenna, an Anritsu MS27102A remote spectrum-monitoring unit, and the ARPA-Lazio Search24 control software [68]. The Keysight N6850A passive antenna [62] is connected to the portable spectrum analyzer via a 1.5 m low-loss coaxial cable. The antenna delivers uniform gain across all licensed cellular bands up to the 3.6 GHz. The weather-proof MS27102A sweeps 9 kHz–6 GHz continuously and, thanks to its internal pre-selector, outputs real-time narrow-band channel power while operating unattended on a rooftop site [69]. Search24 [70] scripts enable streaming the data to a local computer over a dedicated Ethernet link.

2) *Conversion of Received Power to EMF*: The received power for a given frequency channel f at the output of the antenna is measured in dBm. For a given frequency f , the received power is then converted into the electric-field strength (measured in V/m) as given below [2]:

$$E_f = \sqrt{\frac{P_r(f) Z_0}{A_e(f)}} = \sqrt{\frac{10^{\frac{P_{dBm}(f)-30}{10}} Z_0}{A_e(f)}} \quad (24)$$

where $Z_0 \approx 376.73 \Omega$, which is the intrinsic (wave) impedance of free space. For a measurement antenna with linear gain G_f , the effective aperture $A_e(f)$ is defined as follows:

$$A_e(f) = \frac{G_f \lambda_f^2}{4\pi}, \quad \lambda_f = \frac{c}{f}, \quad G_f = \left(\frac{A_{GC}}{\lambda_f \cdot 10^{\alpha_f/20}} \right)^2 \quad (25)$$

where c is the speed of light. A_{GC} is antenna-gain calibration constant. The antenna factor α_f changes as a function of frequency f as in [68], [71].

3) *External Conditions*: User activity patterns, driven by work schedules and lifestyle habits, directly influence device usage and consequently the received power and EMF levels.

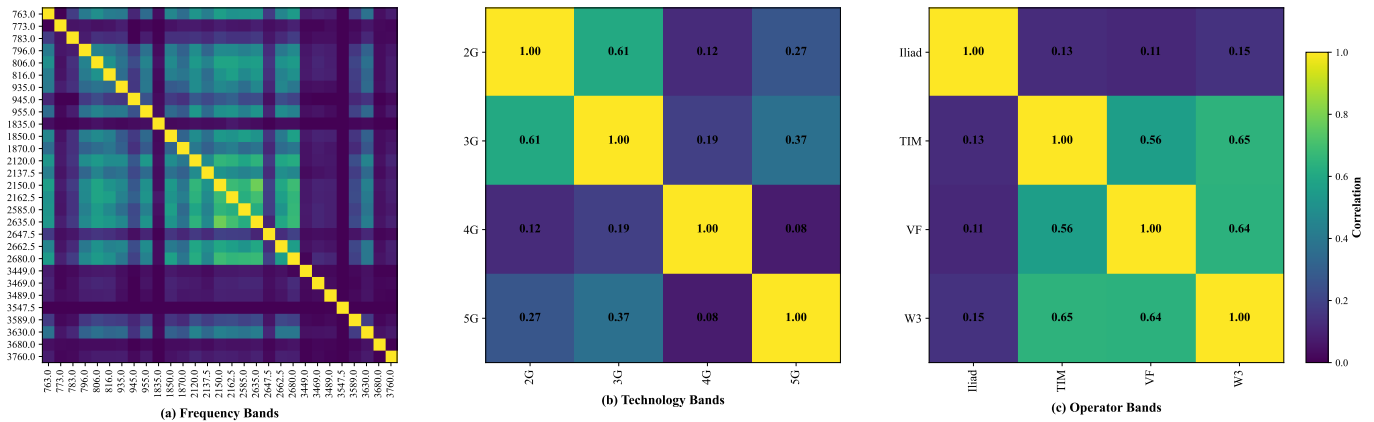


Fig. 5: Correlation maps of EMF levels for (a) frequency bands, (b) cellular technologies, and (c) network operators.

To account for these temporal variations, calendar-based contextual information is incorporated as an external conditioning signal for EMF prediction. For each observation with time stamp t , three features were appended:

- **Italy_WorkingDay** $\in \{0, 1\}$: indicates whether t falls on a weekday (Monday–Friday) and is not listed in the Italian public–holiday calendar.³
- **Italy_WorkingHour** $\in \{0, 1\}$: equals 1 when the local clock time lies inside the standard business window [09:00, 17:00) and 0 otherwise.
- **Italy_Season** $\in \{1, 2, 3, 4\}$: a flag assigned based on the astronomical equinox–solstice boundaries, i.e., 1) *Spring*: March 21 to June 20; 2) *Summer*: June 21 to September 22; 3) *Autumn*: September 23 to December 20; and 4) *Winter*: December 21 to March 20 in the next year.
- **Italy_Multi** $\in \{1, 2, 3, 4\} \times \{0, 1\}$: a two-dimensional multi-condition feature obtained by concatenating Italy_Season and Italy_WorkingDay.

B. EMF Classification and Correlation Analysis

From Table II, the aggregate EMF associated with any given operator or cellular technology can be obtained as follows:

$$E_{\mathcal{F}_\chi}(t) = \left(\sum_{f \in \mathcal{F}_\chi} E_f^2 \right)^{1/2}, \quad (26)$$

where $\mathcal{F}_\chi \in \{2G, 3G, 4G, 5G, TIM, VF, W3, Iliad\}$. As an illustration, the 2G band corresponds to the frequency set $\mathcal{F}_{2G} = \{935.0, 945.0, 955.0\}$ MHz, so the aggregate 2G EMF can be computed as $E_{2G}(t) = \sqrt{E_{935.0}^2 + E_{945.0}^2 + E_{955.0}^2}$.

Fig. 5(a) depicts the correlation of EMF among all frequencies. We note that the EMF levels across the bands (e.g., 700–900 MHz, 1800–2100 MHz, 2.6 GHz, and 3.4–3.8 GHz) tend to be more strongly correlated with each other indicating that exposure dynamics are largely driven by co-located carriers within the same spectral neighbourhood.

³The holiday list covers national and widely observed regional holidays for 2023–2024, including Easter, Liberation Day, Labour Day, Republic Day, Ferragosto, All Saints’ Day, Immaculate Conception, and the Christmas–New Year period. It also includes the university closure date and no teaching activities dates for Università degli Studi di Roma Tor Vergata. [72]

Fig. 5(b) depicts the correlation of EMF observed among the cellular technologies in the Italian dataset. 2G and 3G exhibit the strongest off-diagonal correlation ($\rho \approx 0.61$), reflecting similar temporal usage patterns of legacy technologies at this location. In contrast, 4G is only weakly correlated with the other technologies ($\rho \leq 0.19$), while 5G shows moderate correlation with 2G and 3G ($\rho \approx 0.27$ – 0.37).

The EMF correlation map (Fig. 5(c)) reveals a high correlation among TIM, VF, and W3, with pairwise correlations in the range $\rho \approx 0.56$ – 0.65 , while Iliad remains only weakly correlated with the other operators ($\rho \approx 0.11$ – 0.15). This indicates that the EMF exposure patterns of the three incumbent operators are highly synchronized at the hospital site, whereas Iliad follows a more independent deployment and load profile.

V. NUMERICAL RESULTS AND DISCUSSIONS

This section presents a comprehensive evaluation of the proposed EMFusion model against state-of-the-art benchmarks. To assess forecasting performance, we define both deterministic (point) and probabilistic forecasts metrics followed by the key baselines and evaluation settings.

A. Evaluation Metrics

Let y_i denote the true observed value at time step i , \hat{y}_i the corresponding median (p50) point forecast produced by the model, and m the total number of samples in the test set. In what follows, we describe the point forecast and

1) **Point Forecast Metrics**: evaluate the accuracy of a single predicted value (the median) against the true value. The considered metrics are listed as follows:

- **Mean Absolute Percentage Error (MAPE)**: measures the average percentage difference between the predicted and actual values, and is defined as follows:

$$\text{MAPE} = \frac{100}{m} \sum_{i=1}^m \frac{|y_i - \hat{y}_i|}{|y_i|} \quad (27)$$

TABLE III: A comparative analysis of univariate forecasting performance of EMFusion with imputation without external conditions. Metrics are ordered as CRPS, ND, NRMSE, MAPE, and PICP. Lower is better for CRPS, ND, NRMSE, MAPE; higher is better for PICP. **Bold** = best in column; underline = second best in column.

| Operator-wise Performance | | | | | | | | | | | | | | | | | | | | |
|---------------------------|---------------|---------------|---------------|----------------|--------------|---------------|---------------|---------------|----------------|--------------|---------------|---------------|---------------|----------------|--------------|---------------|---------------|---------------|----------------|--------------|
| Model | Iliad | | | | | TIM | | | | | VF | | | | | W3 | | | | |
| | CRPS | ND | NRMSE | MAPE | PICP | CRPS | ND | NRMSE | MAPE | PICP | CRPS | ND | NRMSE | MAPE | PICP | CRPS | ND | NRMSE | MAPE | PICP |
| NF | 0.0224 | 0.1901 | 0.2271 | 22.0056 | 69.36 | 0.0110 | 0.2674 | 0.3344 | 30.5366 | <u>65.99</u> | 0.0057 | 0.1505 | 0.1899 | 16.3322 | <u>69.26</u> | <u>0.0134</u> | 0.1732 | 0.2126 | 19.5926 | 72.44 |
| IQLSTM | <u>0.0208</u> | 0.1742 | 0.2088 | 22.0082 | <u>69.61</u> | 0.0098 | 0.2272 | 0.2905 | 23.7362 | 65.43 | 0.0060 | 0.1484 | 0.2158 | 16.5989 | 64.66 | 0.0146 | 0.1742 | 0.2179 | 19.3497 | <u>67.87</u> |
| DDPM | 0.0281 | 0.2266 | 0.2752 | 24.7179 | 75.38 | 0.0131 | 0.3078 | 0.4063 | 35.0737 | 76.78 | 0.0067 | 0.1741 | 0.2173 | 19.2858 | 90.22 | 0.0338 | 0.3945 | 0.4217 | 42.9547 | 28.02 |
| VAE | 0.0255 | 0.2040 | 0.2424 | 24.0345 | 54.86 | 0.0121 | 0.2880 | 0.3504 | 33.7195 | 53.63 | 0.0063 | 0.1630 | 0.2040 | 17.8781 | 58.19 | 0.0146 | 0.1842 | 0.2236 | 21.5268 | 66.11 |
| LSTM-Dropout | 0.0311 | 0.2298 | 0.2626 | 32.2884 | 33.07 | 0.0137 | 0.2944 | 0.3334 | 38.0923 | 31.38 | 0.0072 | 0.1687 | 0.2004 | 20.5388 | 31.19 | 0.0232 | 0.2515 | 0.2747 | 34.6254 | 31.17 |
| WGAN | 0.0237 | 0.1856 | 0.2216 | 21.6153 | 50.18 | 0.0207 | 0.3413 | 0.3809 | 44.7403 | 0.00 | <u>0.0055</u> | <u>0.1419</u> | 0.1780 | 15.6357 | 60.28 | 0.0138 | 0.1741 | 0.2096 | 20.5489 | 62.22 |
| TimeGrad (29) | 0.0329 | 0.3405 | 0.8942 | 89.2536 | — | <u>0.0094</u> | 0.4230 | 1.3310 | 52.4586 | — | 0.0084 | 0.2997 | 1.0983 | 29.7099 | — | 0.0203 | 0.3184 | 1.0497 | 48.2214 | — |
| TimeGrad (8)v2 | 0.0552 | 0.1790 | 0.5465 | 26.7691 | — | 0.0271 | 0.3545 | 1.1546 | 34.5811 | — | 0.0201 | 0.1785 | 1.0200 | <u>15.6345</u> | — | 0.0367 | 0.2124 | 0.7484 | 18.9919 | — |
| EMForecaster | 0.0243 | <u>0.1706</u> | <u>0.2019</u> | <u>21.5334</u> | 34.50 | 0.0103 | <u>0.2042</u> | <u>0.2499</u> | <u>22.5550</u> | 29.67 | 0.0061 | <u>0.1419</u> | 0.2031 | 16.0613 | 44.94 | 0.0147 | <u>0.1585</u> | <u>0.1937</u> | <u>18.5124</u> | 37.61 |
| EMFusion | 0.0169 | 0.1304 | 0.1772 | 14.2795 | 50.40 | 0.0067 | 0.1433 | 0.2143 | 14.1847 | 58.51 | 0.0043 | 0.0997 | <u>0.1781</u> | 11.0273 | 52.25 | 0.0099 | 0.1132 | 0.1639 | 12.1131 | 52.19 |

| Technology-band-wise Performance | | | | | | | | | | | | | | | | | | | | |
|----------------------------------|---------------|---------------|---------------|----------------|--------------|---------------|---------------|---------------|----------------|--------------|---------------|---------------|---------------|----------------|--------------|---------------|---------------|---------------|----------------|--------------|
| Model | 2G | | | | | 3G | | | | | 4G | | | | | 5G | | | | |
| | CRPS | ND | NRMSE | MAPE | PICP | CRPS | ND | NRMSE | MAPE | PICP | CRPS | ND | NRMSE | MAPE | PICP | CRPS | ND | NRMSE | MAPE | PICP |
| NF | 0.0028 | 0.1416 | 0.1773 | 14.3473 | 59.79 | 0.0150 | 0.2153 | 0.2534 | 24.2409 | 62.59 | 0.0217 | 0.1637 | 0.1983 | 18.1657 | <u>69.23</u> | <u>0.0024</u> | 0.2103 | 0.3111 | 18.5137 | 72.20 |
| IQLSTM | <u>0.0027</u> | <u>0.1342</u> | 0.1708 | <u>13.7036</u> | 56.70 | <u>0.0134</u> | 0.1841 | 0.2256 | 20.9445 | <u>63.17</u> | 0.0210 | <u>0.1488</u> | <u>0.1827</u> | <u>17.1465</u> | 66.22 | 0.0028 | 0.1901 | <u>0.2994</u> | <u>18.1656</u> | 66.50 |
| DDPM | 0.0029 | 0.1462 | 0.1858 | 15.0905 | 82.02 | 0.0150 | 0.2132 | 0.2536 | 26.5512 | 76.83 | 0.0267 | 0.1890 | 0.2345 | 19.6537 | 74.21 | 0.0031 | 0.2536 | 0.3570 | 24.2072 | <u>71.12</u> |
| VAE | 0.0028 | 0.1429 | 0.1786 | 14.3644 | <u>60.92</u> | 0.0168 | 0.2227 | 0.2606 | 26.1413 | 45.59 | 0.0237 | 0.1698 | 0.2051 | 19.2985 | 58.84 | 0.0028 | 0.2298 | 0.3246 | 21.2987 | 57.09 |
| LSTM-Dropout | 0.0033 | 0.1388 | <u>0.1699</u> | 14.4200 | 32.48 | 0.0196 | 0.2728 | 0.2991 | 44.0706 | 48.00 | 0.0294 | 0.1994 | 0.2273 | 24.2642 | 39.79 | 0.0038 | 0.2742 | 0.3224 | 28.7500 | 14.29 |
| WGAN | 0.0028 | 0.1374 | 0.1747 | 13.7520 | 53.91 | 0.0146 | 0.2003 | 0.2339 | 23.7100 | 54.25 | 0.0224 | 0.1556 | 0.1903 | 17.8671 | 51.53 | 0.0046 | 0.2674 | 0.3303 | 26.9596 | 0.00 |
| TimeGrad (29) | 0.0059 | 0.3761 | 2.2558 | 38.7363 | — | 0.0267 | 0.3133 | 0.9559 | 61.6179 | — | 0.0190 | 0.3375 | 0.9451 | 56.1075 | — | 0.0051 | 0.3912 | 0.9879 | 40.6475 | — |
| TimeGrad (8)v2 | 0.0072 | 0.1746 | 1.9840 | 16.9011 | — | 0.0339 | 0.2040 | 0.6425 | 24.7493 | — | 0.0584 | 0.1888 | 0.6344 | 21.9084 | — | 0.0111 | 0.3741 | 1.0243 | 21.8487 | — |
| EMForecaster | 0.0104 | 0.1682 | 0.2156 | 19.0429 | 37.40 | 0.0139 | <u>0.1688</u> | <u>0.2122</u> | <u>19.6655</u> | 36.68 | 0.0134 | 0.1661 | 0.2102 | 19.3257 | 37.34 | 0.0128 | <u>0.1802</u> | 0.2262 | 20.6762 | 34.69 |
| EMFusion | 0.0016 | 0.0821 | 0.1135 | 8.3460 | 59.64 | 0.0085 | 0.1153 | 0.1564 | 13.1791 | 52.88 | <u>0.0169</u> | 0.1109 | 0.1495 | 11.8418 | 55.69 | 0.0019 | 0.1518 | 0.4311 | 11.5743 | 66.95 |

• **Normalized Deviation (ND):** ND metric measures the total absolute error relative to the total magnitude of the true values, is defined as follows:

$$ND = \frac{\sum_{i=1}^m |y_i - \hat{y}_i|}{\sum_{i=1}^m |y_i|} \quad (28)$$

• **Root Mean Square Error (RMSE) and Normalized RMSE (NRMSE):** RMSE measures the standard deviation of the prediction errors. NRMSE normalizes RMSE by the root mean square of the true values, facilitating comparison across datasets with different scales.

$$RMSE = \sqrt{\frac{1}{m} \sum_{i=1}^m (y_i - \hat{y}_i)^2} \quad (29)$$

$$NRMSE = \frac{RMSE}{\sqrt{\frac{1}{m} \sum_{i=1}^m y_i^2}} \quad (30)$$

2) *Probabilistic Forecast Metrics:* Probabilistic metrics evaluate the quality of the predicted *intervals* and the *full distribution*, assessing both sharpness (the width of the interval) and reliability (the coverage).

• **Prediction Interval Coverage Probability (PICP):** measures the proportion of realized values that fall within the predicted interval. For each forecast horizon step k , let the prediction interval be $PI_\gamma = [L_k, U_k]$, where $\underline{\alpha} = \frac{1-\gamma}{2}$, $\bar{\alpha} = 1 - \underline{\alpha}$. For example, an 80% prediction interval corresponds

to $\gamma = 0.8$, yielding $\underline{\alpha} = 0.1$ and $\bar{\alpha} = 0.9$. Ideally, PI_γ should closely match the target confidence level γ . Define the coverage indicator as follows:

$$c_i = \begin{cases} 1, & \text{if } y_i \in [L_i, U_i], \\ 0, & \text{otherwise.} \end{cases} \quad (31)$$

Over m forecasting values, the PICP is computed as

$$PICP = \frac{1}{m} \sum_{i=1}^m c_i. \quad (32)$$

For reporting in percentage form, $100 \times PICP$ is used. Ideally, $PICP \approx \gamma$, indicating well-calibrated predictive intervals.

• **Continuous Ranked Probability Score (CRPS):** evaluates the quality of the entire predictive distribution by measuring the discrepancy between the predictive CDF F and the observed value y as shown below:

$$CRPS(F, y) = \int_{-\infty}^{\infty} (F(z) - \mathbf{1}\{y \leq z\})^2 dz, \quad (33)$$

where $\mathbf{1}\{\cdot\}$ denotes the indicator function. When only predictive samples $X^{(1)}, \dots, X^{(S)} \sim F$ are available, we approximate F using the empirical CDF, i.e.,

$$\hat{F}(z) = \frac{1}{S} \sum_{s=1}^S \mathbf{1}\{X^{(s)} \leq z\} \quad (34)$$

and compute CRPS at each time step accordingly [73].

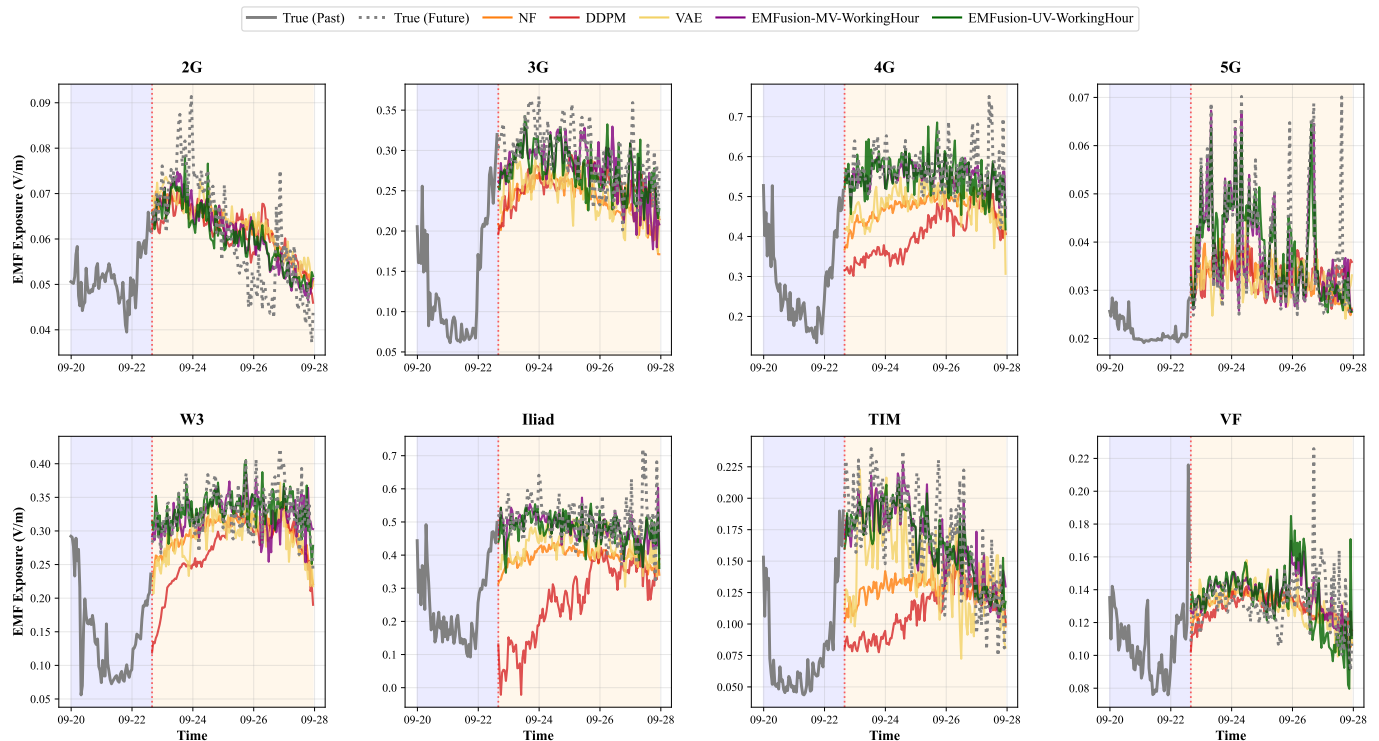


Fig. 6: Comparison of EMF Forecasts in Validation Set Across Technology Bands (Top) and Operators (Bottom)

B. Considered Baselines

To validate the performance of EMFusion, we conduct a comparative analysis against a suite of forecasting models. A brief description⁴ of each baseline model is provided below:

- **DDPM [74]**: the model uses a U-Net denoiser with time-dependent noise embeddings and is trained to match the true forward diffusion process via noise-prediction.
- **WGAN [23]**: the generator maps historical EMF trajectories and latent noise to future EMF scenarios, while the critic enforces distributional realism through the Wasserstein loss with gradient penalty.
- **VAE [75]**: the encoder maps historical EMF sequences into a low-dimensional latent space, and the decoder reconstructs future EMF trajectories from sampled latent variables conditioned on the history. This yields a parametric predictive distribution via the latent Gaussian prior.
- **Normalizing Flow (NF) [74]**: Starting from a base distribution (e.g., multivariate Gaussian), a sequence of invertible transformations is learned to model the joint distribution of future EMF values given the past values, enabling exact likelihood evaluation and sampling.
- **Improved Quantile LSTM (IQLSTM)**: follows [76], where an LSTM-based temporal encoder outputs multiple conditional quantiles of the future EMF distribution. The model is trained using a pinball (quantile) loss over a set

of pre-defined quantile levels, providing a non-parametric representation of forecast uncertainty for each time step.

- **Dropout-based Probabilistic Model**: Following the Monte Carlo Dropout approach of Gal and Ghahramani [77], this algorithm employs a deep LSTM forecaster with dropout layers activated both during training and inference, by running multiple stochastic forward passes with different dropout masks
- **TimeGrad**: TimeGrad [73] is a diffusion-based time-series forecasting model that combines an autoregressive RNN backbone with a conditional diffusion head.

C. Evaluation Settings

All models were trained using an identical training dataset. Their respective hyperparameters were optimized via a grid search procedure on the validation datasets. All algorithms were executed using PyTorch on the Trillium high-performance computing cluster, hosted by SciNet at the University of Toronto. Specifically, we utilized the GPU-accelerated nodes, which are equipped with an AMD EPYC 9654 (Zen 4) 2.4 GHz CPU, 749 GB of system RAM, and four NVIDIA H100 SXM GPUs (80 GB memory each).

In our implementation, each 24-hour period of the EMF time series consists of 192 regularly sampled observations. The model utilizes a 7-day lookback window to forecast the EMF trajectory for the subsequent day. Formally, this configuration yields a historical input window of $H = 1344$ time steps and a forecast horizon of $F = 192$ steps. The dataset is organized into sequential chunks, where each chunk comprises a 7-day lookback window ($H = 1344$) and a 1-day forecast horizon

⁴ The considered baselines are inherently unconditional and do not incorporate external contextual information. For fair comparison, we consider unconditional version of EMFusion (Table III) under identical contextual settings. All EMFusion variants in Tables IV and V share the same backbone architecture, parameter count, optimization settings, and training protocol.

TABLE IV: Forecasting performance of EMFusion without external conditions. Metrics are ordered as CRPS, ND, NRMSE, MAPE, and PICP. Lower is better for CRPS, ND, NRMSE, MAPE; higher is better for PICP. **Bold** = best in row; underline = second best in row. PICP values lower than 10 are considered abnormal and replaced with “-”.

| Metric | Univariate | | | | | Multivariate | | | | | |
|--------|--------------------|--------------------|-----------------------|------------------------|------------------|--------------------|--------------------|-----------------------|------------------------|------------------|--------|
| | EMFusion (Uncond.) | EMFusion (Seasons) | EMFusion (Workingday) | EMFusion (WorkingHour) | EMFusion (multi) | EMFusion (Uncond.) | EMFusion (Seasons) | EMFusion (Workingday) | EMFusion (WorkingHour) | EMFusion (multi) | |
| W3 | CRPS | 0.0099 | 0.0111 | 0.0103 | <u>0.0097</u> | 0.0193 | 0.1096 | 0.1095 | 0.1091 | 0.0086 | 0.0365 |
| | ND | <u>0.1108</u> | 0.1265 | 0.1230 | 0.1156 | 0.2179 | 0.8993 | 0.8950 | 0.8935 | 0.0946 | 0.3300 |
| | NRMSE | <u>0.1601</u> | 0.1708 | 0.1715 | 0.1669 | 0.2673 | 0.9086 | 0.9041 | 0.9028 | 0.1467 | 0.3960 |
| | MAPE | <u>11.79</u> | 14.13 | 13.77 | 12.60 | 25.30 | 88.29 | 87.87 | 87.69 | 9.89 | 38.06 |
| | PICP | 50.49 | 48.91 | <u>54.78</u> | 60.26 | 43.41 | - | - | - | 52.69 | 24.88 |
| Iliad | CRPS | 0.0164 | 0.0173 | 0.0167 | <u>0.0153</u> | 0.0273 | 0.0724 | 0.0724 | 0.0680 | 0.0120 | 0.0435 |
| | ND | 0.1215 | 0.1334 | 0.1319 | <u>0.1211</u> | 0.1975 | 0.4382 | 0.4382 | 0.4041 | 0.0903 | 0.2759 |
| | NRMSE | 0.1744 | 0.1744 | 0.1795 | <u>0.1724</u> | 0.2380 | 0.4819 | 0.4819 | 0.4419 | 0.1469 | 0.3348 |
| | MAPE | 14.05 | 15.94 | 15.05 | <u>13.93</u> | 26.39 | 40.38 | 40.38 | 38.15 | 10.40 | 31.89 |
| | PICP | 50.15 | 52.66 | 53.51 | <u>56.40</u> | 39.08 | 11.37 | 11.37 | 10.76 | 63.02 | 27.86 |
| TIM | CRPS | 0.0066 | 0.0072 | 0.0066 | 0.0063 | 0.0122 | 0.0475 | 0.0475 | 0.0482 | <u>0.0065</u> | 0.0215 |
| | ND | <u>0.1381</u> | 0.1548 | 0.1522 | 0.1466 | 0.2572 | 0.7524 | 0.7524 | 0.7579 | 0.1374 | 0.3891 |
| | NRMSE | 0.2094 | 0.2180 | 0.2254 | 0.2184 | 0.3219 | 0.7756 | 0.7756 | 0.7810 | <u>0.2126</u> | 0.4356 |
| | MAPE | 13.73 | 16.20 | 15.91 | 15.02 | 25.63 | 72.80 | 72.80 | 73.31 | <u>13.81</u> | 43.49 |
| | PICP | 57.05 | 51.81 | <u>57.11</u> | 57.68 | 39.58 | - | - | - | 54.97 | 25.31 |
| VF | CRPS | <u>0.0043</u> | 0.0046 | 0.0044 | <u>0.0043</u> | 0.0077 | 0.0349 | 0.0349 | 0.0331 | 0.0036 | 0.0122 |
| | ND | <u>0.1005</u> | 0.1118 | 0.1078 | 0.1043 | 0.1806 | 0.6308 | 0.6308 | 0.6061 | 0.0826 | 0.2498 |
| | NRMSE | <u>0.1762</u> | 0.1878 | 0.1872 | 0.1862 | 0.2445 | 0.6438 | 0.6438 | 0.6210 | 0.1571 | 0.3039 |
| | MAPE | <u>11.46</u> | 12.35 | 12.15 | 11.74 | 19.34 | 62.48 | 62.48 | 59.82 | 9.67 | 25.23 |
| | PICP | 51.04 | 54.16 | 55.79 | 58.90 | 44.61 | - | - | - | <u>56.56</u> | 29.63 |
| 2G | CRPS | 0.0070 | 0.0076 | 0.0071 | <u>0.0068</u> | 0.0131 | 0.0640 | 0.0639 | 0.0635 | 0.0062 | 0.0234 |
| | ND | <u>0.1165</u> | 0.1310 | 0.1276 | 0.1222 | 0.2186 | 0.7609 | 0.7594 | 0.7525 | 0.1049 | 0.2922 |
| | NRMSE | <u>0.1819</u> | 0.1922 | 0.1947 | 0.1905 | 0.2779 | 0.7760 | 0.7745 | 0.7683 | 0.1721 | 0.3542 |
| | MAPE | <u>12.33</u> | 14.22 | 13.94 | 13.12 | 23.42 | 74.52 | 74.38 | 73.61 | 11.13 | 29.57 |
| | PICP | 52.86 | 51.62 | <u>55.90</u> | 58.95 | 42.53 | - | - | - | 54.74 | 29.04 |
| 3G | CRPS | 0.0093 | 0.0101 | 0.0095 | <u>0.0089</u> | 0.0166 | 0.0661 | 0.0661 | 0.0646 | 0.0077 | 0.0288 |
| | ND | <u>0.1178</u> | 0.1316 | 0.1287 | 0.1219 | 0.2133 | 0.6802 | 0.6791 | 0.6654 | 0.1012 | 0.3200 |
| | NRMSE | <u>0.1800</u> | 0.1877 | 0.1909 | 0.1860 | 0.2679 | 0.7025 | 0.7013 | 0.6867 | 0.1658 | 0.3805 |
| | MAPE | <u>12.76</u> | 14.65 | 14.22 | 13.32 | 24.17 | 65.99 | 65.88 | 64.74 | 10.95 | 38.29 |
| | PICP | 52.18 | 51.88 | 55.30 | 58.31 | 41.67 | - | - | - | <u>56.81</u> | 30.09 |
| 4G | CRPS | 0.0090 | 0.0097 | 0.0092 | <u>0.0086</u> | 0.0162 | 0.0670 | 0.0669 | 0.0655 | 0.0074 | 0.0274 |
| | ND | <u>0.1160</u> | 0.1298 | 0.1268 | 0.1202 | 0.2113 | 0.6923 | 0.6911 | 0.6775 | 0.0994 | 0.2959 |
| | NRMSE | <u>0.1783</u> | 0.1865 | 0.1893 | 0.1847 | 0.2662 | 0.7130 | 0.7117 | 0.6974 | 0.1638 | 0.3536 |
| | MAPE | <u>12.59</u> | 14.45 | 14.04 | 13.16 | 23.90 | 67.33 | 67.21 | 66.03 | 10.78 | 32.58 |
| | PICP | 51.98 | 51.83 | 55.30 | 58.49 | 42.01 | - | - | - | <u>56.50</u> | 28.18 |
| 5G | CRPS | 0.0085 | 0.0091 | 0.0086 | <u>0.0081</u> | 0.0149 | 0.0505 | 0.0505 | 0.0494 | 0.0071 | 0.0241 |
| | ND | <u>0.1246</u> | 0.1387 | 0.1360 | 0.1296 | 0.2231 | 0.6435 | 0.6435 | 0.6315 | 0.1119 | 0.3413 |
| | NRMSE | <u>0.1923</u> | 0.1995 | 0.2044 | 0.1989 | 0.2816 | 0.6692 | 0.6692 | 0.6562 | 0.1823 | 0.3899 |
| | MAPE | <u>13.24</u> | 15.17 | 14.76 | 13.93 | 24.25 | 62.11 | 62.11 | 61.15 | 11.93 | 39.23 |
| | PICP | 53.82 | 52.61 | 55.88 | 57.67 | 40.72 | - | - | - | <u>57.38</u> | 25.59 |

($F = 192$). We allocate 60% of these chunks for training, with 20% reserved for validation and testing, respectively. The PICP confidence level is $\gamma = 80\%$.

To construct the probabilistic prediction intervals during the inference phase, we generate an ensemble of $\hat{N} = 100$ independent scenarios. The structural hyperparameters for EMFusion are optimized to capture complex temporal dependencies. Specifically, the diffusion process is configured with $T = 200$ steps by default, while the U-Net backbone employs a hierarchical depth across its layers, with the dimension expansion factors $[1, 2, 2, 2, 2, 2, 2, 2]$ respectively. For training, we employ a learning rate of 5×10^{-4} and a batch size of 64 over 1500 epochs. The architecture further incorporates an 8-head attention mechanism within a U-Net model of depth 6 to ensure robust feature extraction. Finally, the simulation incorporates essential physical constants, including the free-space wave impedance $Z_0 = 376.73 \Omega$ and the antenna-gain calibration constant $A_{GC} = 9.73$. The training procedure incorporates standard regularization (e.g., early stopping based on validation loss, L_2 regularization, and batch normalization).

D. Performance Evaluation

1) *Comparative Analysis of EMFusion without External Conditions*: **Table-III** analyzes the univariate forecasting performance of the EMFusion model, configured with imputation and without external conditions. We compare it against several baselines, including generative models (NF, DDPM, VAE, WGAN) and other probabilistic forecasting models (IQLSTM, LSTM-Dropout). The evaluation is based on five key metrics, CRPS, ND, NRMSE, and MAPE (where lower is better) and PICP (where higher is better).

In both the operator-wise and technology-band-wise breakdowns, EMFusion consistently achieves the best scores for CRPS, ND, NRMSE, and MAPE, while only WGAN achieves a fractionally better NRMSE for the VF dataset. From the operator perspective, the performance gap is even more pronounced. EMFusion’s CRPS (0.0067) and MAPE (14.18%) are far superior to all baselines in terms of TIM. We also observe EMFusion drastically reduces all error metrics in the 2G 3G and 4G dataset. While 5G dataset appears to be the most challenging, with higher error values for all models. Despite this, EMFusion still delivers the best performance in CRPS (0.0019), ND (0.1518), and MAPE (11.57%).

In terms of evaluation, the highest PICP scores are con-

TABLE V: **Performance comparison** Lower is better for ND, NRMSE, and MAPE; for PICP, a value closest to 80% is preferred. Best per column in **bold**. Reported as mean \pm standard error.

| Method | ND | NRMSE | MAPE | PICP |
|-------------|----------------------------|----------------------------|-----------------------------|-----------------------------|
| NF | 0.1739 \pm 0.0332 | 0.2447 \pm 0.0941 | 18.1875 \pm 2.8910 | 69.1871 \pm 6.0702 |
| IQLSTM | 0.1829 \pm 0.0338 | 0.2575 \pm 0.0954 | 19.2144 \pm 2.6370 | 61.8676 \pm 5.9028 |
| WGAN | 0.1959 \pm 0.0507 | 0.2588 \pm 0.0998 | 21.3099 \pm 4.3154 | 50.0930 \pm 9.8127 |
| VAE | 0.1908 \pm 0.0411 | 0.2597 \pm 0.0971 | 20.6526 \pm 3.8411 | 52.2893 \pm 4.4282 |
| DDPM | 0.1989 \pm 0.0520 | 0.2647 \pm 0.0985 | 22.5219 \pm 6.0977 | 85.9521 \pm 6.4352 |
| Dropout | 0.2418 \pm 0.0481 | 0.2937 \pm 0.0867 | 30.2881 \pm 6.8275 | 27.9310 \pm 6.7606 |
| EMFusion-MV | | | | |
| Uncondition | 0.2486 \pm 0.0688 | 0.3257 \pm 0.1048 | 23.6121 \pm 6.2094 | 33.0397 \pm 10.4381 |
| Multi | 0.2083 \pm 0.0412 | 0.2808 \pm 0.0955 | 22.8826 \pm 5.1239 | 41.6521 \pm 6.5349 |
| WorkingDay | 0.6345 \pm 0.2315 | 0.6705 \pm 0.2088 | 62.0675 \pm 22.9755 | 4.8629 \pm 7.7988 |
| Season | 0.6355 \pm 0.2347 | 0.6735 \pm 0.2123 | 61.9106 \pm 23.5813 | 5.7850 \pm 8.1614 |
| WorkingHour | 0.1049 \pm 0.0241 | 0.1858 \pm 0.0936 | 10.7561 \pm 1.4898 | 56.4799 \pm 5.0838 |

sistently achieved by DDPM and NF. For example, DDPM achieves an exceptional 90.22% for VF and 82.02% for 2G, while NF scores 72.44% for W3. This indicates that these models enable larger percentage of the true (observed) values fall inside the model’s prediction intervals. EMFusion provides a more balanced result, with PICP scores generally in the 50-60% range. This suggests it produces tighter, more accurate prediction intervals that are less conservative but more closely reflect the actual forecast.

Fig. 6 highlights the performance of multivariate EMFusion across all datasets organized by cellular technology bands and operators. Multivariate EMFusion with working hour condition provides the closest match to the ground truth EMF values, i.e., it reproduces the daily exposure cycle, aligns well with the timing of peaks and troughs, and preserves the moderate intra-day variability without following high-frequency noise. Univariate EMFusion with working hour condition exhibits a similar pattern but tends to slightly underestimate the most pronounced peaks in some panels. In contrast, NF and VAE generally produce smoother forecasts that track the overall trend but miss sharp local excursions, leading to significant phase and amplitude mismatches. DDPM is more responsive to transient fluctuations, but this often manifests as spurious oscillations and overfitting to local noise, especially in higher-exposure bands such as 4G and 5G.

2) Univariate vs Multivariate Conditional EMFusion:

Table-IV shows the significance of incorporating appropriate contextual conditions in the reverse diffusion process. In particular, the **WorkingHour**-conditioned EMFusion achieves the lowest CRPS, ND, NRMSE, and MAPE regardless of the operator (W3, Iliad, TIM, VF) or technology band (2G–5G). The multi-conditioned multivariate model (last column) does not surpass the **WorkingHour**-only model, suggesting that fine-grained time-of-day conditioning captures most of the useful temporal structure for EMF exposure, while additional context yields diminishing returns. From the operator perspective, TIM and VF benefit strongly from conditional diffusion: for example, under multivariate modeling their CRPS and MAPE values under EMFusion (**WorkingHour**) are an order of magnitude smaller than uncondition EMFusion, indicating substantially sharper and more accurate forecasts.

Table IV shows a clear dominance of **WorkingHour** conditioning, while multi-conditioning often yields diminishing or negative returns. This reflects the characteristics of the Univer-

sity Hospital site, where EMF exposure closely follows visitor activity with a regular diurnal pattern, strong daytime peaks and low nighttime levels. As a result, **WorkingHour** captures the dominant temporal structure of BS power allocation and explains most of the variance in this dataset. Contextual relevance, however, is environment-dependent. In residential areas, traffic peaks may shift to evenings and weekends, increasing the importance of **WorkingDay** or holiday-related features. The performance degradation observed under multi-conditioning suggests that expanding the conditioning space without sufficient diversity in the training data can reduce learning efficiency. Higher-dimensional conditioning requires adequate coverage of contextual state combinations; when certain states (e.g., **WorkingDay**) are underrepresented in the dataset, the cross-attention mechanism struggles to prioritize the most informative signals.

From the technology-band viewpoint, EMFusion sharply reduces all error metrics for legacy bands (2G, 3G, 4G), with the largest relative gains observed for 4G, where EMFusion (**WorkingHour**) approximately halves the CRPS and MAPE compared to unconditioned EMFusion in the multivariate setting. The 5G band remains the most challenging case, with uniformly higher errors across all models due to its more volatile traffic and deployment patterns. Nonetheless, EMFusion still delivers the best multivariate performance in CRPS, ND, and MAPE for 5G, indicating that the diffusion-based approach remains robust even under rapidly fluctuating EMF dynamics. In terms of interval quality, unconditioned EMFusion exhibits very low PICP values in the multivariate case, reflecting overly narrow and under-dispersed prediction intervals. EMFusion, by contrast, achieves PICP values predominantly in the 50-65% range across operators and bands, with the **WorkingHour** configuration again performing best. Although these values are below the ideal 80% target, they indicate tighter, less conservative intervals that are more informative than those from unconditioned EMFusion.

Table-V reports the forecasting performance of all methods, averaged over all carriers and technologies. The proposed **EMFusion-MV-WorkingHour** consistently outperforms across all error- and distribution-based scores, indicating sharper and better-calibrated predictive distributions. Although its PICP is slightly lower than that of DDPM, it remains competitive with the strongest baselines while delivering substantially improved overall forecasting quality.

3) *Inference Complexity Analysis*: Given a look-back window of length H , a forecast horizon F , an embedding dimension d , and T total diffusion steps, we analyze the inference complexity as shown below. The inference complexity is dominated by the T iterative denoising steps within the U-Net backbone and the cross-attention mechanism. For each denoising step, the complexity of the convolutional layers and attention projections scales with the total sequence length $(H + F)$ and the number of variates N . Specifically, the complexity of a single denoising step in our multivariate architecture is $\mathcal{O}(N \cdot (H + F) \cdot d^2)$. Consequently, the total inference complexity for generating a multivariate forecast scales as $\mathcal{T}_{\text{inference}} = \mathcal{O}(T \cdot N \cdot (H + F) \cdot d^2)$. The inference time for EMFusion is in the order of milliseconds.

TABLE VI: Ablation study on diffusion step size and U-Net depth in EMFusion. The training times reported in the tables are formatted as **HH:MM:SS**, where **HH**, **MM** and **SS** represents the number of hours, minutes, seconds, respectively.

| Setting | ND | NRMSE | MAPE | PICP | Time | |
|-----------------|-----|---------------|---------------|--------------|-------|-----------------|
| Diffusion Steps | 50 | 0.2393 | 0.3963 | 31.62 | 56.94 | 01:32:20 |
| | 200 | 0.1335 | 0.2660 | 15.44 | 65.29 | 02:02:41 |
| | 300 | 0.1759 | 0.3310 | 22.81 | 68.08 | 02:10:18 |
| U-Net Depth | 3 | 0.1786 | 0.3343 | 22.53 | 73.98 | 02:27:50 |
| | 7 | 0.1872 | 0.3393 | 25.92 | 72.03 | 02:51:08 |
| | 9 | 0.1625 | 0.3246 | 19.03 | 62.70 | 03:01:51 |

TABLE VII: Rolling window evaluation for EMFusion.

| Period | ND | NRMSE | MAPE | PICP |
|----------------------------------|--------|--------|-------|-------|
| 2023/07/26 – 2023/12/12 | 0.1510 | 0.2040 | 20.25 | 55.17 |
| 2023/08/25 – 2024/01/11 | 0.1741 | 0.2374 | 18.16 | 56.69 |
| 2023/09/24 – 2024/02/10 | 0.1390 | 0.1954 | 15.84 | 59.76 |
| 2023/10/24 – 2024/03/12 | 0.1959 | 0.3737 | 21.96 | 61.17 |
| Average | 0.1650 | 0.2526 | 19.05 | 58.20 |
| Full Dataset (No rolling window) | 0.1335 | 0.2660 | 15.44 | 65.29 |

4) *Ablation Studies*: In **Table VI**, we varied the diffusion step size $\{50, 200, 300\}$ while fixing the U-Net depth at 8. Also, we investigated the impact of the U-Net backbone depth across $\{3, 7, 9\}$ layers while maintaining a fixed diffusion step size of 50. Overall, performance variations across 50–300 steps are relatively small, indicating that the model is not highly sensitive to the diffusion steps. However, the depth of UNet architecture does impact the performance, i.e., the model with 9 layers outperform. This is because the deeper the model, the larger its receptive field across the entire time series, enabling it to capture abstract information within long sequences at the expense of additional complexity.

To evaluate the framework’s stability across distinct temporal segments, we then performed a rolling-window evaluation by sliding 5-month window across the 8-month period. The results in **Table VII** demonstrate consistent performance, confirming that EMFusion remains robust to the temporal variations. We note that the reduction in training data length inherent in the rolling-window setup can slightly impact performance; for instance, the average MAPE increases from 15.44% to 19.05% compared to the full dataset. This marginal degradation is attributed to the limited training data available within a window.

To address the risk of potential overfitting, **Fig. 7** illustrates the training and validation loss trajectories. The synchronized downward trend and stable convergence of both metrics demonstrate consistent generalization to unseen data without significant divergence. The model also includes explicit regularization through L_2 weight decay and Group Normalization, which help control model capacity and stabilize training. In addition, the diffusion objective perturbs inputs with Gaussian noise at multiple levels while sharing parameters across diffusion steps, introducing an implicit regularization effect that encourages robustness across noise conditions.

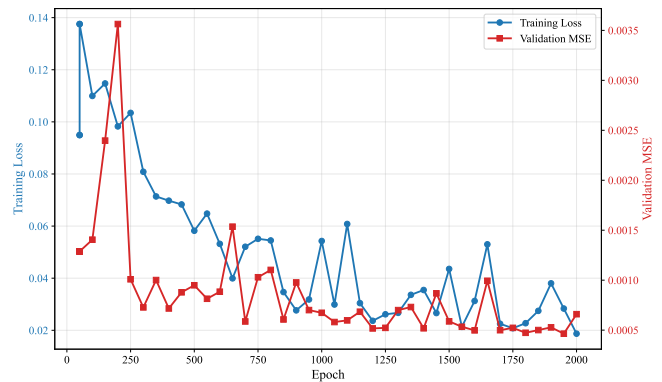


Fig. 7: Training and validation loss across 2000 epochs for the W3 dataset.

E. Ethical and Deployment Considerations

1) *Data Governance*: Reliable EMF forecasting requires robust data governance. In this study, data acquisition and analysis were conducted by the same organization, and the raw datasets were released as open source to ensure transparency and reproducibility. In multi-agency settings, strict compliance with regulations such as the General Data Protection Regulation (GDPR) [78] is essential, including the obfuscation of sensitive metadata and secure data-sharing protocols to prevent unauthorized access or misuse.

2) *Mitigating Monitoring Biases*: Long-term monitoring can suffer from sampling biases due to sensor outages or irregular measurement intervals. EMFusion addresses this through its imputation-based sampling strategy (Section III-D), treating missing data as a structural inpainting task to preserve temporal coherence. While this reduces algorithmic bias, future monitoring systems should incorporate hardware-level detectors to identify abnormal sensor behavior or drift and maintain data reliability.

3) *Scalability for Nationwide Deployment*: Nationwide deployment requires balancing computational overhead with monitoring density. The inference complexity of EMFusion scales linearly with the forecast horizon, $\mathcal{O}(F)$, enabling proactive management in large-scale deployments. However, national implementation also requires infrastructure for real-time data ingestion and long-term cloud storage.

VI. CONCLUSION

This paper introduced EMFusion, a conditional diffusion based probabilistic forecasting framework. The framework employs conditional embeddings, cross-attention based context integration, and imputation-based sampling to improve temporal coherence. Experiments have been conducted on real-world EMF dataset which showed that EMFusion achieved lower deterministic forecasting errors and better probabilistic calibration than representative deep learning time-series and generative baselines. EMFusion is a general data-driven forecasting framework that can be adapted to other locations if monitoring datasets and contextual information are available. Integrating principled data governance and scalable computational architectures will be important for transitioning

EMFusion from a research framework to a reliable tool for nationwide regulatory compliance and public health monitoring. Future extensions may incorporate BS location, transmit power, and user distribution as additional conditioning variables to further tighten forecast distributions. Meta-heuristic optimization methods can also be applied for hyperparameter tuning to obtain more robust EMF forecasts [79].

ACKNOWLEDGMENT

The authors would like to thank Dr. Daniele Franci and Settimio Pavoncello for providing the EMF measurement hardware used to collect the Italian dataset.

REFERENCES

- [1] S. Bani Melhem, H. Tabassum, L. Chiaraviglio, and U. Trang Nguyen, "Joint coverage and EMF compliance analysis in RIS-assisted terahertz networks with optimized RIS deployment," *IEEE Open J. Commun. Soc.*, vol. 6, pp. 8816–8834, 2025.
- [2] L. Chiaraviglio, A. Elzanaty, and M.-S. Alouini, "Health risks associated with 5G exposure: A view from the communications engineering perspective," *IEEE Open J. Commun. Soc.*, vol. 2, pp. 2131–2179, 2021.
- [3] International Commission on Non-Ionizing Radiation Protection (IC-NIRP), *Guidelines for limiting exposure to electromagnetic fields (100 kHz to 300 GHz)*, 2020.
- [4] L. Chiaraviglio, C. Lodovisi, D. Franci, E. Grillo, S. Pavoncello, T. Aureli, N. Blefari-Melazzi, and M.-S. Alouini, "How much exposure from 5g towers is radiated over children, teenagers, schools and hospitals?" *IEEE Open Journal of the Communications Society*, vol. 3, pp. 1592–1614, 2022.
- [5] X. Mootoo, H. Tabassum, and L. Chiaraviglio, "EMForecaster: A deep learning framework for time series forecasting in wireless networks with distribution-free uncertainty quantification," *IEEE Trans. on Netw. Science and Eng.*, vol. 13, pp. 1207–1225, 2026.
- [6] R. Stam, "Comparison of international policies on electromagnetic fields: (power frequency and radiofrequency fields)," National Institute for Public Health and the Environment (RIVM), Netherlands, Tech. Rep., 2018.
- [7] Y. A. Sambo, M. Al-Imari, F. Hélot, and M. A. Imran, "Electromagnetic emission-aware schedulers for the uplink of ofdm wireless communication systems," pp. 1313–1323, 2016.
- [8] H. Jiang, L. You, A. Elzanaty, J. Wang, W. Wang, X. Gao, and M.-S. Alouini, "Rate-splitting multiple access for uplink massive mimo with electromagnetic exposure constraints," *IEEE J. Sel. Areas Commun.*, vol. 41, no. 5, pp. 1383–1397, 2023.
- [9] H. Ibraiwish, A. Elzanaty, Y. H. Al-Badarnah, and M.-S. Alouini, "EMF-aware cellular networks in ris-assisted environments," *IEEE Commun. Lett.*, vol. 26, no. 1, pp. 123–127, 2021.
- [10] L. Chiaraviglio, A. S. Cacciapuoti, G. Di Martino, M. Fiore, M. Montesano, D. Trucchi, and N. B. Melazzi, "Planning 5G networks under EMF constraints: State of the art and vision," *IEEE Access*, vol. 6, pp. 51 021–51 037, 2018.
- [11] International Telecommunication Union, "Guidance on complying with limits for human exposure to electromagnetic fields," <https://www.itu.int/rec/T-REC-K.Sup14-201909-I>, 2019.
- [12] M. Matalatala, M. Deruyck, E. Tanghe, S. Goudos, L. Martens, and W. Joseph, "Joint optimization towards power consumption and electromagnetic exposure for massive MIMO 5G networks," in *Proc. IEEE 29th Annu. Int. Symp. Pers., Indoor, Mobile Radio Commun. (PIMRC)*, 2018, pp. 1208–1214.
- [13] D. Ying, D. J. Love, and B. M. Hochwald, "Beamformer optimization with a constraint on user electromagnetic radiation exposure," in *Proc. 47th Annu. Conf. Inf. Sci. Syst. (CISS)*, 2013, pp. 1–6.
- [14] J. P. B. Nadas, O. Onireti, R. Demo Souza, H. Alves, G. Brante, and M. A. Imran, "Reducing EMF emissions in ultra-reliable low-latency communications with HARQ," *IET Commun.*, vol. 13, no. 20, pp. 2502–2509, 2019.
- [15] D. Franci, S. Coltellacci, E. Grillo, S. Pavoncello, T. Aureli, R. Cintoli, and M. D. Migliore, "Experimental procedure for fifth generation (5G) electromagnetic field (EMF) measurement and maximum power extrapolation for human exposure assessment," *Environments*, vol. 7, no. 3, p. 22, 2020.
- [16] M. D. Migliore, D. Franci, S. Pavoncello, T. Aureli, E. Merli, C. Lodovisi, L. Chiaraviglio, and F. Schettino, "Application of the maximum power extrapolation procedure for human exposure assessment to 5G millimeter waves: Challenges and possible solutions," *IEEE Access*, vol. 10, pp. 103 438–103 446, 2022.
- [17] IEC 62232:2025 — *Determination of RF field strength, power density and specific absorption rate (SAR) in the vicinity of radiocommunication stations — Procedures for assessing maximum permissible exposure (MPE)*, International Electrotechnical Commission (IEC) Std. IEC 62 232:2025, 2025. [Online]. Available: <https://webstore.iec.ch/en/publication/89073>
- [18] S. Iakovidis, A. Manassas, C. Apostolidis, and T. Samaras, "5G EMF exposure at 3.6 GHz in Greece using data from frequency-selective monitoring sensors," *Bioelectromagnetics*, vol. 46, no. 4, p. e70008, 2025.
- [19] Y. Kiouvrekis, I. Givisis, T. Panagiotakopoulos, I. Tsilikas, A. Ploussi, E. Spyrtou, and E. P. Efstathopoulos, "A comparative analysis of explainable artificial intelligence models for electric field strength prediction over eight european cities," *Sensors*, vol. 25, no. 1, p. 53, 2024.
- [20] Z. Pala, "Examining EMF time series using prediction algorithms with R," *IEEE Can. J. Elect. Comput. Eng.*, vol. 44, no. 2, pp. 223–227, 2021.
- [21] C. Nguyen, A. A. Cheema, C. Kurnaz, A. Rahimian, C. Brennan, and T. Q. Duong, "Deep learning models for time-series forecasting of RF-EMF in wireless networks," *IEEE Open J. Commun. Soc.*, vol. 5, pp. 1399–1414, 2024.
- [22] A. Al-Jumaily, A. Sali, M. Riyadh, S. Q. Wali, L. Li, and A. F. Osman, "Machine learning modeling for radiofrequency electromagnetic fields (RF-EMF) signals from mmWave 5G signals," *IEEE Access*, vol. 11, pp. 79 648–79 658, 2023.
- [23] Y. Huang, J. Pei, L. Chen, Z. Du, J. Chen, and Z. Peng, "Probabilistic Net Load Forecasting for High-Penetration RES Grids Utilizing Enhanced Conditional Diffusion Model," *arXiv preprint arXiv:2503.17770*, 2025.
- [24] J. Sohl-Dickstein, E. Weiss, N. Maheswaranathan, and S. Ganguli, "Deep unsupervised learning using nonequilibrium thermodynamics," in *Proc. Int. Conf. Mach. Learn.*, 2015, pp. 2256–2265.
- [25] J. Ho, A. Jain, and P. Abbeel, "Denosing diffusion probabilistic models," in *Adv. Neural Inf. Process. Syst.*, vol. 33, 2020, pp. 6840–6851.
- [26] J. Pei, J. Wang, D. Shi, and P. Wang, "Detection and imputation based two-stage denoising diffusion power system measurement recovery under cyber-physical uncertainties," *IEEE Trans. Smart Grid*, vol. 15, no. 6, pp. 5965–5980, Nov. 2024.
- [27] J. Pei, C. Feng, P. Wang, H. Tabassum, and D. Shi, "Latent diffusion model-enabled low-latency semantic communication in the presence of semantic ambiguities and wireless channel noises," *IEEE Trans. Wireless Commun.*, vol. 24, no. 5, pp. 4055–4072, May 2025.
- [28] A. Borovykh, S. Bohte, and C. W. Oosterlee, "Conditional time series forecasting with convolutional neural networks," *arXiv preprint arXiv:1703.04691*, 2017.
- [29] A. Y. Nikraves, S. A. Ajila, C.-H. Lung, and W. Ding, "Mobile network traffic prediction using MLP, MLPWD, and SVM," in *Proc. IEEE Int. Congr. Big Data (BigData Congress)*, 2016, pp. 402–409.
- [30] M. Di Mauro, G. Galatro, F. Postiglione, W. Song, and A. Liotta, "Multivariate time series characterization and forecasting of VoIP traffic in real mobile networks," *IEEE Trans. on Netw. and Service Manage.*, vol. 21, no. 1, pp. 851–865, 2023.
- [31] A. Dalgkitis, M. Louta, and G. T. Karetos, "Traffic forecasting in cellular networks using the LSTM RNN," in *Proc. of the 22nd Pan-Hellenic conference on informatics*, 2018, pp. 28–33.
- [32] M. A. Habib, P. E. I. Rivera, Y. Ozcan, M. Elsayed, M. Bavand, R. Gaigalas, and M. Erol-Kantarci, "Transformer-based wireless traffic prediction and network optimization in o-ran," in *Proc. IEEE Int. Conf. Commun. Wkshps. (ICC Wkshps.)*, 2024, pp. 1–6.
- [33] C. Fiandrino, E. P. Gómez, P. F. Pérez, H. Mohammadalizadeh, M. Fiore, and J. Widmer, "AIChronoLens: advancing explainability for time series AI forecasting in mobile networks," in *Proc. IEEE Int. Conf. Comput. Commun. (INFOCOM)*, 2024, pp. 1521–1530.
- [34] D. P. Isravel, S. Silas, J. W. Kathrine, E. B. Rajsingh, and J. Andrew, "Multivariate forecasting of network traffic in SDN-based ubiquitous healthcare system," *IEEE Open J. of the Commun. Soc.*, vol. 5, pp. 1537–1550, 2024.
- [35] S. P. Sone, J. J. Lehtomäki, and Z. Khan, "Wireless traffic usage forecasting using real enterprise network data: Analysis and methods," *IEEE Open J. of the Commun. Soc.*, vol. 1, pp. 777–797, 2020.
- [36] Y. Zhang, Y. Wu, A. Liu, X. Xia, T. Pan, and X. Liu, "Deep learning-based channel prediction for LEO satellite massive MIMO communication system," *IEEE Wireless Commun. Lett.*, vol. 10, no. 8, pp. 1835–1839, 2021.

- [37] A. Hameed, J. Violos, A. Leivadreas, N. Santi, R. Grünblatt, and N. Mitton, "Toward QoS prediction based on temporal transformers for IoT applications," *IEEE Trans. on Netw. and Service Manage.*, vol. 19, no. 4, pp. 4010–4027, 2022.
- [38] H. E. Dinaki, S. Shirmohammadi, E. Janulewicz, and D. Côté, "Forecasting video QoE with deep learning from multivariate time-series," *IEEE Open J. of Signal Process.*, vol. 2, pp. 512–521, 2021.
- [39] A. G. Colpitts and B. R. Petersen, "Short-term multivariate KPI forecasting in rural fixed wireless LTE networks," *IEEE Netw. Lett.*, vol. 5, no. 1, pp. 11–15, 2023.
- [40] E. Zhang, Z. Liu, Y. Xiang, and Y. Qu, "Probabilistic QoS metric forecasting in delay-tolerant networks using conditional diffusion models on latent dynamics," *arXiv preprint arXiv:2504.08821*, 2025.
- [41] X. Song, W. Feng, C. Yang, N. Djuric, D. Kljajic, and S. Djuric, "Study on field strength prediction using different models on time series from urban continuous RF-EMF monitoring," *Expert Syst. Appl.*, vol. 274, p. 126963, 2025.
- [42] M. R. Bakcan *et al.*, "Measurement and prediction of electromagnetic radiation exposure level in a university campus," *Tehnički vjesnik*, vol. 29, no. 2, pp. 449–455, 2022.
- [43] G. E. P. Box, G. M. Jenkins, G. C. Reinsel, and G. M. Ljung, *Time Series Analysis: Forecasting and Control*, 5th ed. Hoboken, NJ: John Wiley & Sons, 2015.
- [44] P. De Lellis, F. L. Judice, and N. Pasquino, "Time-series-based model and validation for prediction of exposure to wideband radio frequency electromagnetic radiation," *IEEE Trans. Instrum. Meas.*, vol. 69, no. 6, pp. 3198–3205, 2019.
- [45] Y. Li, X. Lu, Y. Wang, and D. Dou, "Generative time series forecasting with diffusion, denoise, and disentanglement," *Adv. Neural Inf. Process. Syst.*, vol. 35, pp. 23 009–23 022, 2022.
- [46] I. J. Goodfellow, J. Pouget-Abadie, M. Mirza, B. Xu, D. Warde-Farley, S. Ozair, A. Courville, and Y. Bengio, "Generative adversarial nets," *Adv. Neural Inf. Process. Syst.*, vol. 27, 2014.
- [47] A. Koochali, A. Dengel, and S. Ahmed, "If you like it, gan it—probabilistic multivariate times series forecast with gan," *Eng. Proc.*, vol. 5, no. 1, p. 40, 2021.
- [48] Y. Song and S. Ermon, "Generative modeling by estimating gradients of the data distribution," in *Adv. Neural Inf. Process. Syst.*, vol. 32, 2019.
- [49] K. Rasul, C. Seward, I. Schuster, and R. Vollgraf, "Autoregressive denoising diffusion models for multivariate probabilistic time series forecasting," in *Proc. Int. Conf. Mach. Learn.*, 2021, pp. 8857–8868.
- [50] Y. Tashiro, J. Song, Y. Song, and S. Ermon, "CSDI: Conditional Score-based Diffusion Models for Probabilistic Time Series Imputation," in *Adv. Neural Inf. Process. Syst.*, vol. 34, 2021, pp. 24 804–24 816.
- [51] J. M. L. Alcaraz and N. Strodthoff, "Diffusion-based time series imputation and forecasting with structured state space models," *arXiv preprint arXiv:2208.09399*, 2022.
- [52] Z. Yan, J. Pei, H. Wu, H. Tabassum, and P. Wang, "Semantic-aware adaptive video streaming using latent diffusion models for wireless networks," *IEEE Wireless Commun.*, vol. 32, no. 5, pp. 30–38, 2025.
- [53] M. Kollovich, A. F. Ansari, M. Bohlke-Schneider, J. Zschiegner, H. Wang, and Y. B. Wang, "Predict, refine, synthesize: Self-guiding diffusion models for probabilistic time series forecasting," *Adv. Neural Inf. Process. Syst.*, vol. 36, pp. 28 341–28 364, 2023.
- [54] X. Yuan and Y. Qiao, "Diffusion-ts: Interpretable diffusion for general time series generation," *arXiv preprint arXiv:2403.01742*, 2024.
- [55] J. Liu, L. Yang, H. Li, and S. Hong, "Retrieval-augmented diffusion models for time series forecasting," *Adv. Neural Inf. Process. Syst.*, vol. 37, pp. 2766–2786, 2024.
- [56] L. Shen, W. Chen, and J. Kwok, "Multi-resolution diffusion models for time series forecasting," in *Proc. Int. Conf. Learn. Represent.*, 2024.
- [57] Q. Li, Z. Zhang, L. Yao, Z. Li, T. Zhong, and Y. Zhang, "Diffusion-based decoupled deterministic and uncertain framework for probabilistic multivariate time series forecasting," in *Proc. Int. Conf. Learn. Represent.*, 2025.
- [58] C. Meijer and L. Y. Chen, "The rise of diffusion models in time-series forecasting," *arXiv preprint arXiv:2401.03006*, 2024.
- [59] C. Su, Z. Cai, Y. Tian, Z. Zheng, and Y. Song, "Diffusion Models for Time Series Forecasting: A Survey," *arXiv preprint arXiv:2507.14507*, 2025.
- [60] J. Ho, A. Jain, and P. Abbeel, "Denoising Diffusion Probabilistic Models," in *Adv. Neural Inf. Process. Syst.*, vol. 33, 2020.
- [61] J. Ho and T. Salimans, "Classifier-free diffusion guidance," in *Proc. NeurIPS 2021 Workshop on Deep Generative Models and Downstream Appl.*, 2021. [Online]. Available: <https://openreview.net/forum?id=qw8AKxfYbl>
- [62] Keysight Technologies. (2025) N6850A broadband omnidirectional antenna. [Online]. Available: <https://www.keysight.com/ca/en/product/N6850A/broadband-omnidirectional-antenna.html>
- [63] O. Ronneberger, P. Fischer, and T. Brox, "U-net: Convolutional networks for biomedical image segmentation," in *Proc. Int. Conf. Med. Image Comput. Comput.-Assist. Interv. (MICCAI)*, 2015, pp. 234–241.
- [64] K. He, X. Zhang, S. Ren, and J. Sun, "Deep residual learning for image recognition," in *Proc. IEEE Conf. Comput. Vis. Pattern Recognit. (CVPR)*, 2016, pp. 770–778.
- [65] A. Vaswani, N. Shazeer, N. Parmar, J. Uszkoreit, L. Jones, A. N. Gomez, L. Kaiser, and I. Polosukhin, "Attention Is All You Need," in *Adv. Neural Inf. Process. Syst.*, vol. 30, 2017, pp. 5998–6008.
- [66] R. Rombach, A. Blattmann, D. Lorenz, P. Esser, and B. Ommer, "High-resolution image synthesis with latent diffusion models," in *Proc. IEEE Conf. Comput. Vis. Pattern Recognit. (CVPR)*, 2022, pp. 10 674–10 685.
- [67] O. Petit, N. Thome, C. Rambour, L. Themyr, T. Collins, and L. Soler, "U-net transformer: Self and cross attention for medical image segmentation," in *Int. Workshop on Mach. Learn. in Medical Imaging*, 2021, pp. 267–276.
- [68] L. Chiaraviglio, C. Lodovisi, D. Franci, S. Pavoncello, and T. Aureli, "Six months in the life of a cellular tower: Is 5G exposure higher than pre-5G one?" in *Proc. IEEE Int. Symp. Meas. Netw.* IEEE, 2022, pp. 1–6.
- [69] Anritsu Company. (2022) Remote spectrum monitor MS27102A. [Online]. Available: <https://www.anritsu.com/en-us/test-measurement/products/ms27102a>
- [70] ARPA Lazio. (2017) Search24 — software for remote control of non-vector spectrum analyzers. [Online]. Available: https://www.airp-asso.it/wp-content/uploads/convegni/2017_Salerno/Atti%20Salerno%202017.pdf
- [71] Keysight Technologies, "Antenna factor N6850A," <https://www.keysight.com/main/redirector.jsp?action=ref&ckey=3104458&cname=EDITORIAL>, 2025, excel data file.
- [72] Università degli Studi di Roma "Tor Vergata". (2025, 3) Academic Calendar 2024–2025. [Online]. Available: <https://web.uniroma2.it/en/contenuto/academic-calendar>
- [73] K. Rasul, C. Seward, I. Schuster, and R. Vollgraf, "Autoregressive Denoising Diffusion Models for Multivariate Probabilistic Time Series Forecasting," in *Proc. Int. Conf. Mach. Learn.*, vol. 139. PMLR, 2021.
- [74] E. H. Capel and J. Dumas, "Denoising diffusion probabilistic models for probabilistic energy forecasting," in *Proc. IEEE Belgrade PowerTech, Belgrade, Serbia*, 2023, pp. 1–6.
- [75] S. R. Khazeinyasab, R. Iyengar, and W. L. Leow, "Probabilistic individual short-term load forecasting using conditional variational autoencoder," in *Proc. IEEE Power Energy Soc. Gen. Meet. (PESGM)*, Orlando, FL, USA, 2023, pp. 1–5.
- [76] Q. Huang and S. Wei, "Improved quantile convolutional neural network with two-stage training for daily-ahead probabilistic forecasting of photovoltaic power," *Energy Conv. Manag.*, vol. 220, p. 113085, Sep. 2020.
- [77] Y. Gal and Z. Ghahramani, "Dropout as a bayesian approximation: Representing model uncertainty in deep learning," in *Proc. Int. Conf. Mach. Learn.*, vol. 48, 2016, pp. 1050–1059.
- [78] European Parliament and Council of the European Union. (2016) Regulation (EU) 2016/679 of the European Parliament and of the Council of 27 April 2016 on the protection of natural persons with regard to the processing of personal data and on the free movement of such data (General Data Protection Regulation). Official Journal of the European Union, L 119, 4 May 2016, pp. 1-88. [Online]. Available: <https://eur-lex.europa.eu/eli/reg/2016/679/oj>
- [79] E.-S. M. El-Kenawy, S. Mirjalili, N. Khodadadi, A. A. Abdelhamid, M. M. Eid, M. El-Said, and A. Ibrahim, "Feature selection in wind speed forecasting systems based on meta-heuristic optimization," *PLOS ONE*, vol. 18, no. 2, p. e0278491, 2023.